Gondwana Research 54 (2018) 81–101

Contents lists available at ScienceDirect

Gondwana Research

journal homepage: www.elsevier.com/locate/gr

Anatomy of impactites and shocked zircon grains from Dhala reveals Paleoproterozoic meteorite impact in the Archean basement rocks of Central India

Shan-Shan Li [a], S. Keerthy [b], M. Santosh [a,c], S.P. Singh [d], C.D. Deering [e], M. Satyanarayanan [f], M.N. Praveen [g], V. Aneeshkumar [b], G.K. Indu [b], Y. Anilkumar [b], K.S. Sajinkumar [b,e,*]

[a] School of Earth Science and Resources, China University of Geosciences, Beijing 100083, China
[b] Department of Geology, University of Kerala, Thiruvananthapuram 695581, Kerala, India
[c] Centre for Tectonics, Resources and Exploration, Department of Earth Sciences, University of Adelaide, SA 5005, Australia
[d] Department of Geology, Bundelkhand University, Jhansi 284128, India
[e] Department of Geological & Mining Engineering & Sciences, Michigan Technological University, Houghton, MI 49931, USA
[f] CSIR-National Geophysical Research Institute, Hyderabad 500007, India
[g] Geological Survey of India, Bangalore 560078, India

ARTICLE INFO

Article history:
Received 31 May 2017
Received in revised form 26 September 2017
Accepted 27 October 2017
Available online 31 October 2017

Handling Editor: S. Kwon

Keywords:
Dhala Impact Structure
Reidite
Planar Fracture
Zircon U-Pb geochronology
K_2O metasomatism

ABSTRACT

The Dhala structure in Central India has been a topic of global interest ever since the report of an ancient meteorite impact event there. Here we present an integrated study of the petrology, geochemistry, and zircon U-Pb zircon geochronology and rare earth element geochemistry from the structure along with and an analysis of the grain morphology and textural features. Our results provide new insight into the nature and timing of the impact event. The zircon grains from the impactites show textures typical of shock deformation which we correlate with the impact event. We also identified the presence of reidite based on Raman spectroscopy and characteristics such as a persistent planar fracture, bright backscattered electron images, and a lack of zoning, which are all diagnostic features of this mineral formed during an impact event. Our zircon U-Pb data from the various rock types in the basement show magma emplacement at ca. 2.5–2.47 Ga, and the Pb loss features suggest that the impact might have occurred between ca. 2.44 Ga and ca. 2.24 Ga. Another minor group of late Paleoproterozoic zircons with concordant ages of 1826 and 1767 Ma in the brecciated quartz reefs along the margins of the impact crater from unfractured grains represent an younger thermal event after the impact. The rare-earth element patterns of the Neoarchean to early Paleoproterozoic zircon population reflect the effects of hydrothermal alteration on a peralkaline host rock. The abnormally high concentration of K_2O in the impactite (up to 15.91 wt%), is also consistent with metasomatic alteration associated with the impact event.

© 2017 International Association for Gondwana Research. Published by Elsevier B.V. All rights reserved.

1. Introduction

The Earth's surface has long been subjected to bombardment by meteorites, asteroids, and comets with recent models emphasizing the importance of such impacts in providing bio-elements to early Earth (Maruyama and Ebisuzaki, 2016). Because of the geologically active nature of Earth, the manifestations of many of the early cratering events have been largely erased, with only rare evidence preserved. So far, around 190 impact craters/structures have been confirmed on Earth (http://www.unb.ca/passc/ImpactDatabase/). The study of impact craters provides insight into a number of geological and biological aspects of the Earth's evolution, such as: 1) the formation of large circular geological structures, 2) the origin of major crustal deformation events, 3) important economic mineral and hydrocarbon deposits, 4) the origin of extensive ejecta deposits and marine breccias, 5) major biological extinction (French and Koeberl, 2010), and 6). Impact events in the early history of the Earth are also considered as important triggers of tectonic processes in the proto-crust (Santosh et al., 2017; Maruyama et al., 2016; Maruyama and Santosh, 2017, and references therein).

The Dhala Impact Structure in Central India, carved out within the Archean Bundelkhand Craton, was considered to be formed through caldera collapse (e.g., Jain et al., 2001; Srivastava and Nambiar, 2003; Rao et al., 2005) but this region gained interest ever since a meteorite impact was suggested by Pati (2005). Identifying and characterizing impact

* Corresponding author at: Department of Geology, University of Kerala, Thiruvananthapuram 695581, Kerala, India.
E-mail address: skochapp@mtu.edu (K.S. Sajinkumar).

https://doi.org/10.1016/j.gr.2017.10.006
1342-937X/© 2017 International Association for Gondwana Research. Published by Elsevier B.V. All rights reserved.

structures in an Archean terrane is particularly a formidable task because of the deterioration of the typical impact morphology by active denudational processes combined with deposition of sediments. This is exemplified in the case of the Dhala Impact Structure where the raised rim was eroded away and the central depression was filled with the Proterozoic Vindhyan sediments. Moreover, the meteorite itself is completely destroyed in an impact event and hence diagnostic indicators of this event are found only in the terrestrial target rocks, which are often subjected to the extreme pressure and temperature environment of intense shock waves generated by the impact (Melosh, 1989).

Petrological and geochemical investigations of the impacted rocks and identification of diagnostic minerals are the conventional methods employed to identify meteorite impacts (Koeberl et al., 2012). High concentration of platinum group of elements were reported by Alvarez et al. (1980) in the thin clay layer that marks the K-T boundary, correlated to impact event. Several other works have also shown the importance of petrologic and geochemical information in characterizing impactites and target rocks (e.g., Koeberl et al., 1998; Mittlefehldt et al., 2005; Osae et al., 2005; Koeberl, 2007; Bermúdez et al., 2016; Silva et al., 2016).

Zircon, a common accessory mineral in most of the terrestrial rocks, is an ideal mineral that might preserve diagnostic impact fingerprints, especially in Precambrian terranes. Due to its resistance to thermal, chemical and mechanical break-down, the mineral has long been employed to decipher the timings of complex geological processes including impact events (Blum, 1993). The studies of Krogh et al. (1984, 1993a, 1993b) showed that zircon crystals present in impactites can survive the impact and provide insights into the impact event even in the absence of impact glass. Zircon grains preserve shock features even under granulite facies metamorphic conditions (Reimold et al., 2002). In particular, there are several distinct features of shock waves such as: 1) Planar Deformation Features (PDF), 2) granular texture, 3) Pb loss (e.g., Glass, 2002; Wittmann et al., 2006; Kalleson et al., 2009), 4) twinning, 5) polymorphism, and 6) trace element patterns (Timms et al., 2017). The shock induced zircon will lose some of its radiogenic lead (Pb loss) and in some cases yield distinct ages (Blum, 1993), with the upper intercept in the U-Pb concordia corresponding to the primary age of the impactites and lower intercept denoting the age of the impact event. However, lower intercept ages for the impact event can rarely be derived from older zircons. Therefore, signs of severe Pb loss supplemented with textural features revealed by cathodoluminescence (CL), backscattered electron (BSE), and/or reflected light images, have been used to identify zircon in impact structures (Krogh et al., 1984; Krogh et al., 1993a, 1993b; Kamo et al., 1996; Gibson et al., 1997; Bowring et al., 1998; Reimold et al., 2002; Glass, 2002; Wittmann et al., 2006; Kalleson et al., 2009).

This study investigates the characteristics of an impact event through the examination of the petrology and geochemistry of impactites, including an analysis of shocked zircons by CL, BSE, and reflected light imaging techniques, Laser Raman and U-Pb dating as rare earth element (REE) patterns. Our results provide new insight into a major deformational event associated with the formation of the Dhala Impact Structure.

2. Geologic background

The Dhala Impact Structure occurs within the Bundelkhand Craton, one of the Precambrian cratonic nuclei of India (Fig. 1a). The craton is dominantly composed of Mesoarchean to Paleoproterozoic crystalline rocks, and is bordered by the NE-SW trending Great Boundary Fault (GBF) in the west, ENE-WSW trending Son- Narmada Faults in the south, the Singhbhum Craton in the east and NW-SE trending Yamuna

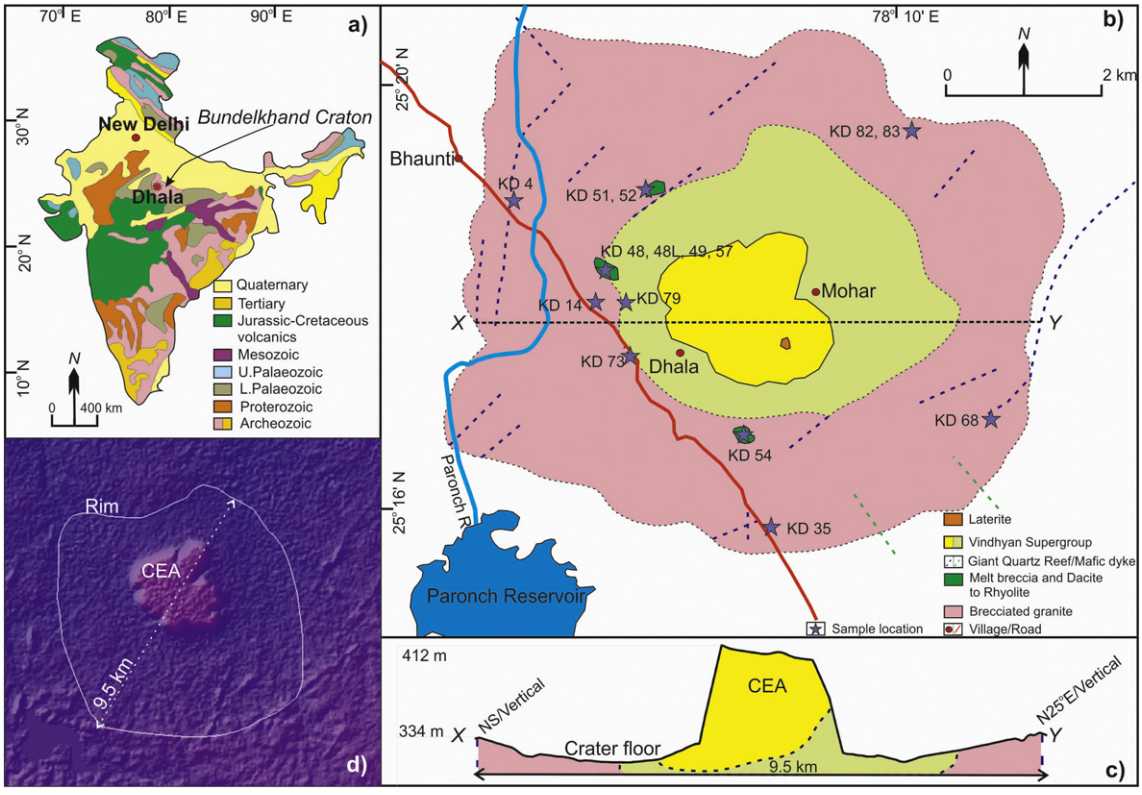


Fig. 1. Location map of the study area. (a) Geological map of India showing broad geological set-up. (b) Geological map of the study area. The inner rim is suspected to be the boundary of Vindhyan sediments whereas the outer rim at several places coincides with Giant Quartz Reefs (c) cross section of the crater created from Google Earth imagery. The minor undulations seen in the crater floor are whaleback structures of brecciated granite (d) Hill shade map of Dhala derived from 30 m spatial resolution SRTM data. The elevated area can be well observed with a characteristic elevation difference when compared to the eroded rims.
(Panel a: Source: Geological Survey of India, 1998; panel b: Modified after Bhattacharya et al., 2006)

Fault in the north (Bhattacharya and Singh, 2013; Mondal et al., 2002; Kumar et al., 2011; Mohan et al., 2012). The Mesoarchean and Paleoproterozoic rocks are grouped as the Bundelkhand Gneissic Complex (BGC), composed of the Bundelkhand granitoids together with enclaves and slivers of low- to high-grade metamorphic supracrustals rocks of calc-silicate and quartzofeldspathic affinity, tonalite-trondhjemite-granodiorite gneiss (TTG), metavolcanics, and mafic and ultramafic rocks (Roy et al., 2014). The greenstone belt (metavolcanics, and mafic and ultramafics rocks) (Singh and Dwivedi, 2015; Verma et al., 2016) formed during the Neoproterozoic and have been considered to represent the earliest mantle plume arc accretion in the central part of Bundelkhand Craton (Mondal et al., 2002; Saha et al., 2016; Verma et al., 2016). The Archean granitoid-greenstone sequence is intruded by Neoarchean granitoids and early Proterozoic mafic dike swarms (Rao et al., 2005), which remain largely undeformed (Basu, 1986; Sharma and Rahman, 2000; Pati et al., 2007; Singh et al., 2007). These granitoids are characterized by medium to coarse grained biotite granite, leucogranite, gray granite, pink granite and hornblende granite (Singh et al., 2010). The development of giant quartz reefs and mafic dike swarms of early Proterozoic were also identified (Singh and Bhattacharya, 2017), marking the final stage of cratonization, with the growth and transformation of the Archean crust into the Bundelkhand craton (Singh and Dwivedi, 2015; Ray et al., 2016).

The Dhala Structure is an eroded remnant of a ~9.5 km diameter impact structure characterized by outcrops of granites, brecciated granite, impact melt rocks comprising melt breccia and dacite to rhyolite type felsic rocks with brecciated mafic dikes and quartz reef (Fig. 1b). Based on lithology and textures, the Dhala structure has been divided

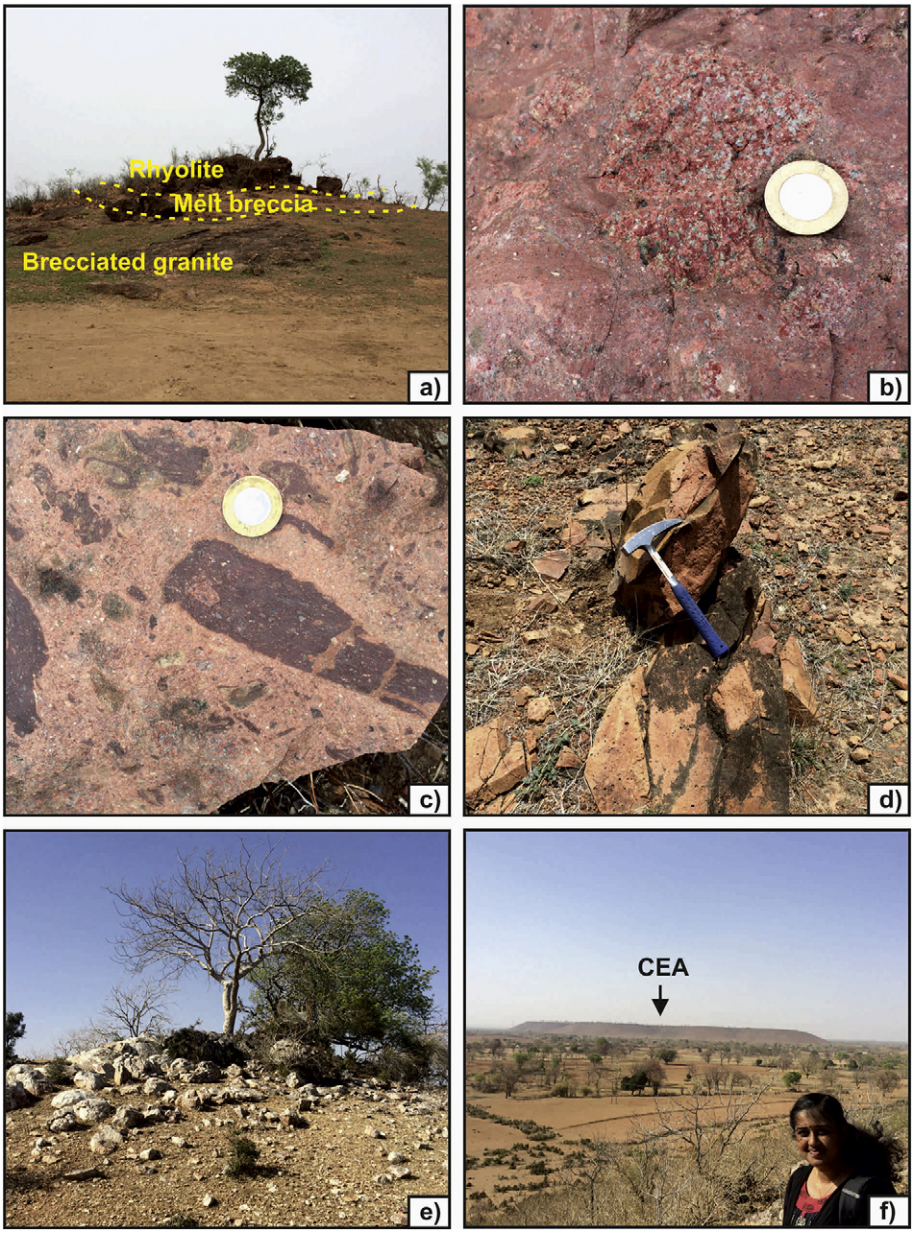


Fig. 2. Field photographs of different lithounits in Dhala (a) Rhyolite, melt breccia and brecciated granite seen in sequence in a small hillock. This top to bottom sequence represents the order of decrease in severity of impact event. (b) Brecciated granite showing different size of clasts. Usually the clasts range from a few mm to a few meters. The clasts and groundmass of the breccias show an intense pink colour due to the presence of K-feldspars (c) Melt breccia showing clasts of glassy material and a light coloured fine grained matrix with granite clasts (d) Fine grained dacite to rhyolite rock with vesicles and showing a charred appearance. On close observation with a hand-lens these rocks also show the presence of angular clasts similar to the melt breccias. (e) Giant Quartz Reef often seen emplaced along the rim shows a buff colour. The randomly distributed boulders are obvious feature of quartz reef, otherwise too, it is brecciated at several locations (f) 'CEA' seen from a distant view. The elevated neck-like mesa structure represents a remnant of regional denudation or an event of uplift.

into two parts viz. (i) outer/rim part: dominated by varieties of brecciated rocks and (ii) the inner/central part: dominated by granite breccias and Vindhyan sediments. The central depression, filled with Vindhyan sediments (Proterozoic), has been termed 'central elevated area' (CEA) by Pati et al. (2008) and the authors differ from the concept of 'CEA'. The crater lacks a raised rim (Fig. 1c). Laterite occupies a portion of this elevated area and occurs as a mound. The elevated area stands out prominently in the 30 m spatial resolution Shuttle Radar Topographic Mission (SRTM) data (Fig. 1d). The outer rim was extrapolated in a GIS environment using several criss-cross profiles through the crater. At several places, the outer rim location coincides with giant quartz reef outcrops.

The above stratigraphic sequence (Fig. 2a) also suggests an impact event rather than a volcanic caldera/magmatic chamber collapse. The unbrecciated basement granite in the inner/central part is not exposed, but has been intercepted during drilling of 4 and 76 holes by the Geological Survey of India (GSI) and Atomic Minerals Division (AMD), respectively, in this area (Roy et al., 2014). Brecciated granite constitutes the most widespread lithounit covering the entire crater floor and at places forms whaleback hillocks (Pati et al., 2008). This rock is characterized by clasts of varying size and shape (Fig. 2b). The clasts and groundmass of the breccia show an intense dark pink to cherry red colour representing K_2O metasomatism and fluidization. The clasts contain larger grains of K-feldspar and quartz whereas the groundmass is medium to fine grained and rich in K-feldspar. The pervasive pink colour of the matrix indicates the presence of secondary hydrothermal K-feldspar. This lithounit was termed a monomict breccia by Pati et al. (2008). The outer boundary of the crater is marked by the disappearance of this brecciated granite. Melt breccia and dacite to rhyolite occurs together, with melt breccia overlain by rhyolite, and has been identified in three locations as small patchy outcrops. Melt breccia has clasts of different rocks including the basement granite and tachylite (Fig. 2c). The clasts in melt breccia range in size from millimeter to several tens of centimeters (up to 30 cm) and show a variety of shapes from rounded to angular to raft shaped. Many clasts show evidence for partial digestion in the melt-groundmass. Brecciation is the most common manifestation of impact events and in Dhala it is visible both at the macro- and micro-scales. The formation of brecciated granite, melt breccia, and brecciated dacite to rhyolite, which are common in the study area, correspond to macro-scale brecciation. In this case, the host rock (impactite) itself forms both the matrix and clasts. Development of primary and secondary K-feldspar in the target rocks has been documented from several

Table 1
Whole rock geochemical data for the samples collected from Dhala.

Sample no.	KD-4	KD-14	KD-35	KD-48	KD-48L	KD-49	KD-51	KD-52	KD-54	KD-57	KD-68	KD-73	KD-79	KD-82	KD-83
Major elements (wt%)															
SiO_2	94.88	69.89	69.30	67.59	67.79	67.58	74.77	72.13	65.96	68.33	71.05	73.49	67.22	64.95	69.14
Al_2O_3	0.79	13.89	9.77	10.01	11.62	9.61	8.46	10.29	11.67	11.11	9.89	12.49	11.17	10.87	11.76
Fe_2O_3	0.67	1.75	4.64	6.02	1.91	5.94	1.89	0.72	3.36	1.88	1.92	2.10	3.26	5.37	1.73
MnO	0.00	0.02	0.06	0.01	0.00	0.06	0.01	0.01	0.02	0.05	0.01	0.03	0.03	0.06	0.01
MgO	0.20	1.69	2.64	0.36	1.04	0.60	0.67	0.28	3.24	0.95	1.38	0.20	2.16	7.00	0.95
CaO	0.16	0.42	3.02	0.25	0.29	0.25	0.55	0.24	0.77	1.27	0.20	1.74	0.33	0.65	0.36
Na_2O	1.17	2.72	3.20	1.13	1.09	1.09	1.59	1.14	1.13	1.11	1.16	2.73	1.08	1.97	1.15
K_2O	0.20	7.83	5.00	15.53	15.91	14.96	10.41	15.33	13.71	14.08	13.77	5.78	14.75	7.19	14.35
TiO_2	0.01	0.48	0.53	0.47	0.54	0.46	0.64	0.39	0.53	0.49	0.01	0.02	0.47	0.77	0.44
P_2O_5	0.01	0.12	0.15	0.08	0.08	0.09	0.09	0.07	0.12	0.10	0.02	0.01	0.07	0.16	0.04
LOI	2.20	1.34	2.11	1.75	0.58	1.10	1.18	0.50	0.49	0.92	0.71	1.82	0.56	1.42	0.12
Sum	100.29	100.15	100.42	103.20	100.85	101.74	100.26	101.10	101.00	100.29	100.12	100.41	101.10	100.41	100.05
Trace elements (ppm)															
Sc	0.61	6.19	12.08	6.48	8.99	7.12	7.08	5.36	3.65	7.58	2.09	1.53	6.82	8.16	4.97
V	4.60	42.60	94.13	52.37	26.64	49.81	26.86	34.06	12.35	31.35	35.27	10.85	35.76	46.67	23.39
Cr	5.15	15.79	66.61	51.92	40.39	50.09	41.25	38.54	20.90	34.83	20.12	17.21	23.82	37.27	13.43
Co	2.03	5.41	16.77	4.36	2.34	7.29	3.42	2.40	2.51	3.40	2.89	1.64	15.84	16.84	3.93
Ni	4.76	5.14	9.73	18.91	10.96	28.36	15.00	7.56	10.85	11.66	4.89	4.36	38.56	9.44	6.78
Cu	1.07	2.13	2.40	2.69	3.91	2.05	4.19	4.79	2.80	2.05	1.51	1.67	1.51	2.65	1.51
Zn	19.87	52.58	65.16	30.12	20.64	35.06	28.43	45.16	18.97	39.16	38.07	16.59	44.42	70.84	22.22
Ga	1.69	21.76	29.92	17.84	19.51	13.97	11.91	11.85	9.28	18.05	10.34	11.98	23.51	21.58	18.07
Rb	6.01	231.25	206.19	252.73	232.72	204.20	204.62	202.47	175.46	231.15	338.78	226.21	146.71	172.34	206.77
Sr	14.64	84.61	423.91	27.52	13.75	20.53	54.75	36.48	27.25	27.95	67.75	31.83	27.47	125.72	40.34
Y	1.56	19.63	28.87	36.84	29.03	31.04	19.53	31.95	12.68	29.69	11.29	29.85	26.37	16.94	21.69
Zr	28.18	412.12	344.66	340.97	295.62	315.13	271.99	292.22	164.04	309.89	151.06	131.02	361.66	307.99	296.29
Nb	1.10	18.60	16.48	16.13	14.42	15.69	13.35	13.81	9.32	14.64	2.25	19.01	15.06	14.03	12.65
Cs	0.14	4.09	4.89	1.31	3.46	0.99	0.86	1.26	0.50	3.91	2.74	1.53	1.00	7.61	1.20
Ba	21.33	761.68	1020.61	572.63	470.45	761.30	550.11	588.26	531.45	712.18	1859.36	129.57	525.78	729.07	1032.55
La	3.86	96.34	49.64	111.26	38.86	52.75	29.46	44.99	18.24	33.13	9.49	4.73	105.99	28.59	75.46
Ce	7.63	178.90	89.79	204.72	74.39	94.94	54.57	78.07	33.60	61.67	17.02	7.80	197.75	53.38	109.76
Pr	0.87	20.54	11.78	23.62	8.81	11.73	6.84	9.77	4.15	7.69	2.12	1.10	20.87	7.20	16.68
Nd	2.54	59.13	37.64	71.95	27.48	35.59	21.14	30.83	12.59	24.05	6.72	3.61	59.85	23.93	50.61
Sm	0.38	8.80	6.84	11.74	5.24	6.06	3.91	5.88	2.29	4.74	1.42	1.25	8.62	4.38	8.54
Eu	0.06	1.20	1.36	1.82	0.91	0.90	0.73	1.31	0.48	0.77	0.48	0.30	1.43	0.96	1.63
Gd	0.27	5.14	5.05	8.24	4.09	4.66	2.85	4.35	1.71	3.75	1.27	1.78	5.37	2.89	5.42
Tb	0.04	0.69	0.72	1.11	0.65	0.70	0.45	0.71	0.28	0.61	0.22	0.42	0.75	0.44	0.74
Dy	0.20	2.96	3.56	4.81	3.79	3.68	2.61	4.25	1.61	3.66	1.43	3.53	3.48	2.33	3.35
Ho	0.04	0.63	0.73	1.00	0.79	0.77	0.55	0.93	0.34	0.78	0.31	0.77	0.73	0.50	0.65
Er	0.11	1.63	1.84	2.56	1.98	1.98	1.40	2.50	0.88	2.06	0.81	2.07	1.89	1.33	1.53
Tm	0.02	0.28	0.29	0.40	0.32	0.31	0.23	0.44	0.14	0.34	0.14	0.34	0.31	0.22	0.23
Yb	0.12	2.12	1.92	2.80	2.17	2.15	1.62	3.28	1.00	2.37	1.14	2.34	2.25	1.58	1.56
Lu	0.02	0.35	0.30	0.45	0.35	0.34	0.28	0.56	0.16	0.38	0.23	0.36	0.36	0.26	0.25
Hf	0.50	9.98	6.22	7.66	7.47	6.30	7.10	8.56	4.20	7.82	6.05	5.90	8.56	6.55	7.28
Ta	0.09	1.36	1.37	1.46	1.41	1.35	1.06	1.18	1.31	1.62	0.46	2.08	1.45	1.16	1.30
Pb	7.58	30.81	33.82	22.41	9.91	16.20	24.57	22.75	12.43	24.97	26.29	21.82	19.47	17.85	12.88
Th	2.10	37.34	17.16	21.97	23.41	16.33	26.19	22.37	16.63	24.68	31.58	12.53	28.70	10.83	22.58
U	0.76	3.10	4.39	7.18	4.05	3.85	6.06	5.36	2.87	5.29	4.10	3.41	7.49	2.22	3.67

terrestrial impact craters (e.g. Schmieder et al., 2010) resulting in potassic alteration of the impactites. The dacite to rhyolite are fine-grained and display a highly vesicular and charred appearance (Fig. 2d). On close observation these rocks also show the presence of angular clasts similar to the melt breccia.

Recently Pati et al. (2016) examined borehole data and characterized a new unit called 'pseudotachylitic breccia', a non-genetic term for a melt rock containing lithic and mineral clasts associated with impact structure. This unit occurs as veins and pods and differs from the brecciated granite in having mafic clasts. The NE-SW trending quartz

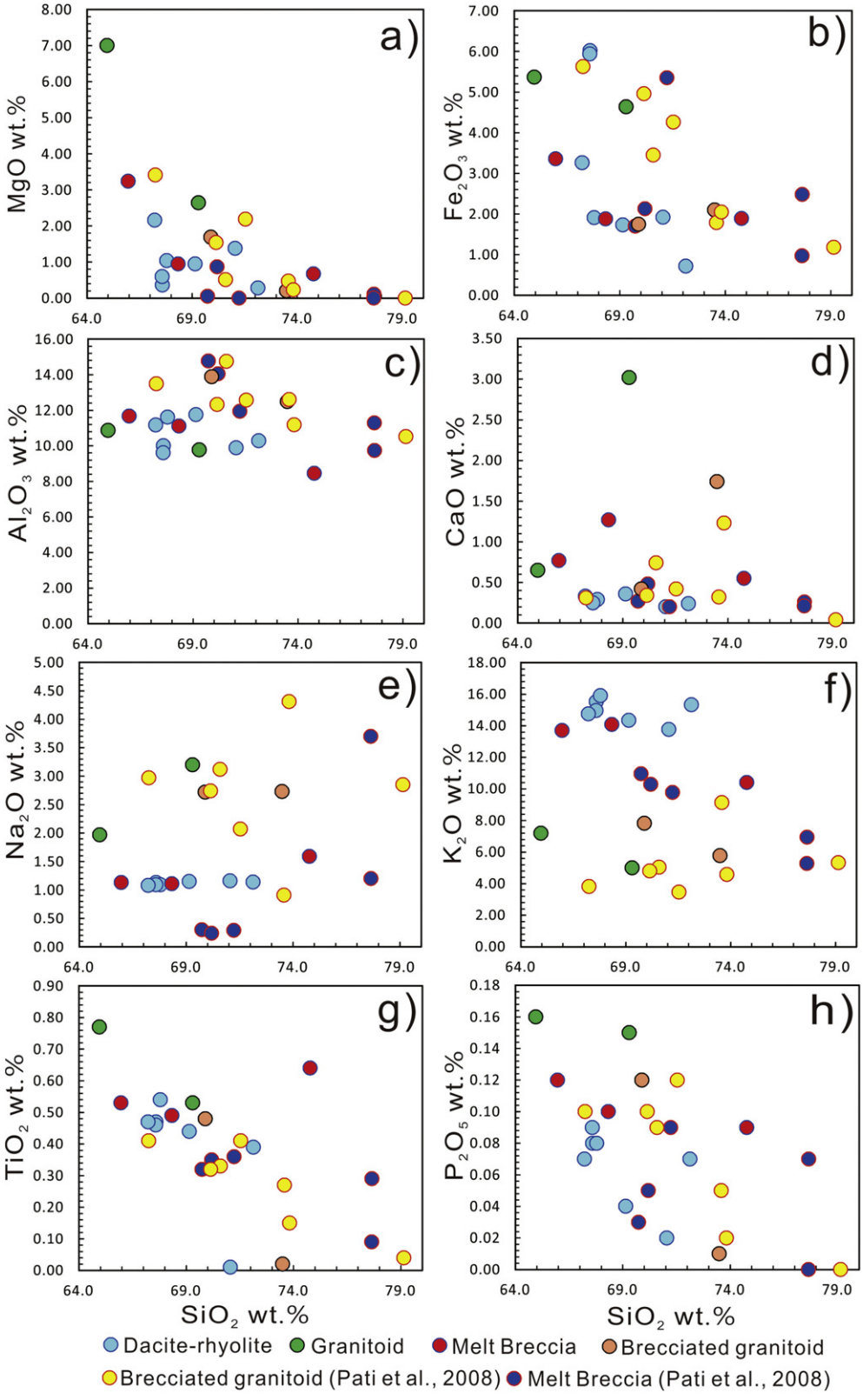


Fig. 3. Harker diagram for SiO_2 versus several major oxides. The major element geochemistry shows similar trend indicating a same parentage for all the lithounits of the study area.

reefs are buff coloured and form prominent ridges (Fig. 2e). The mafic dikes cut across the granite and have the same trend as the quartz reef. These dikes are fine grained and resemble the Malwa plateau basalts occurring southwest of the Bundelkhand Craton (Sharma and Rahman, 2000).The Vindhyan sediments occupy the central depression, which is now elevated to form a 'CEA' like structure (Fig. 2f) either due to uplift or regional denudation.

3. Analytical methods

3.1. Major and trace element geochemistry of impactites

Fifteen fresh rock samples (shown in Fig. 1b) from the Dhala Impact Structure were collected for geochemical analyses. A summary of the samples analyzed in this study is given in Appendix A (supplementary material). The rocks were initially prepared for geochemical analysis using a jaw crusher followed by manual reduction to fine powder in an agate mortar. The major elements were determined by X-ray Fluorescence (XRF) (Phillips®MAGIX PROModel 2440), with a relative standard deviation of <3% (Krishna et al., 2007). For trace elements, including rare earth elements (REE) and high field strength elements (HFSE), the sample powders were dissolved in reagent grade HF:HNO_3 acid mixture in Savillexscrew top vessels. Solutions were analyzed by High Resolution Inductively Coupled Plasma Mass Spectrometry (HR-ICP-MS) (Nu ATTOM®, Nu Instruments, UK) at the CSIR-National Geophysical Research Institute, Hyderabad. ^{103}Rh was used as an internal standard for correcting internal drift. External drift was corrected by repeated analyses of a set of geochemical reference materials G-2 (USGS), AC-E (GIT-IWG, France), JG-1a and JG-2 (GSJ, Japan) (Govindaraju, 1994; GEOREM, georem.mpch-mainz.gwdg.de), which were also used as calibration standards. Appendix B (supplementary material) shows the accuracy and precision obtained for individual analysis. Anomalies of HFSE relative to neighboring REE are given as Nb/Nb*, Zr/Zr*, Hf/Hf* and Ti/Ti*. Mg# is calculated as $Mg/(Mg + Fe_{total})$. The trace element data were normalized according to Sun and McDonough (1989). The detailed methods of sample decomposition techniques and analysis, as well as instrument parameters and precision are as reported in Manikyamba et al. (2015).

3.2. Petrography

Petrographic studies were conducted using an Olympus CX 31 U-TVO 5XC-3 SN-5JO1650 and Olympus BX51-P BX2 Series microscopes,

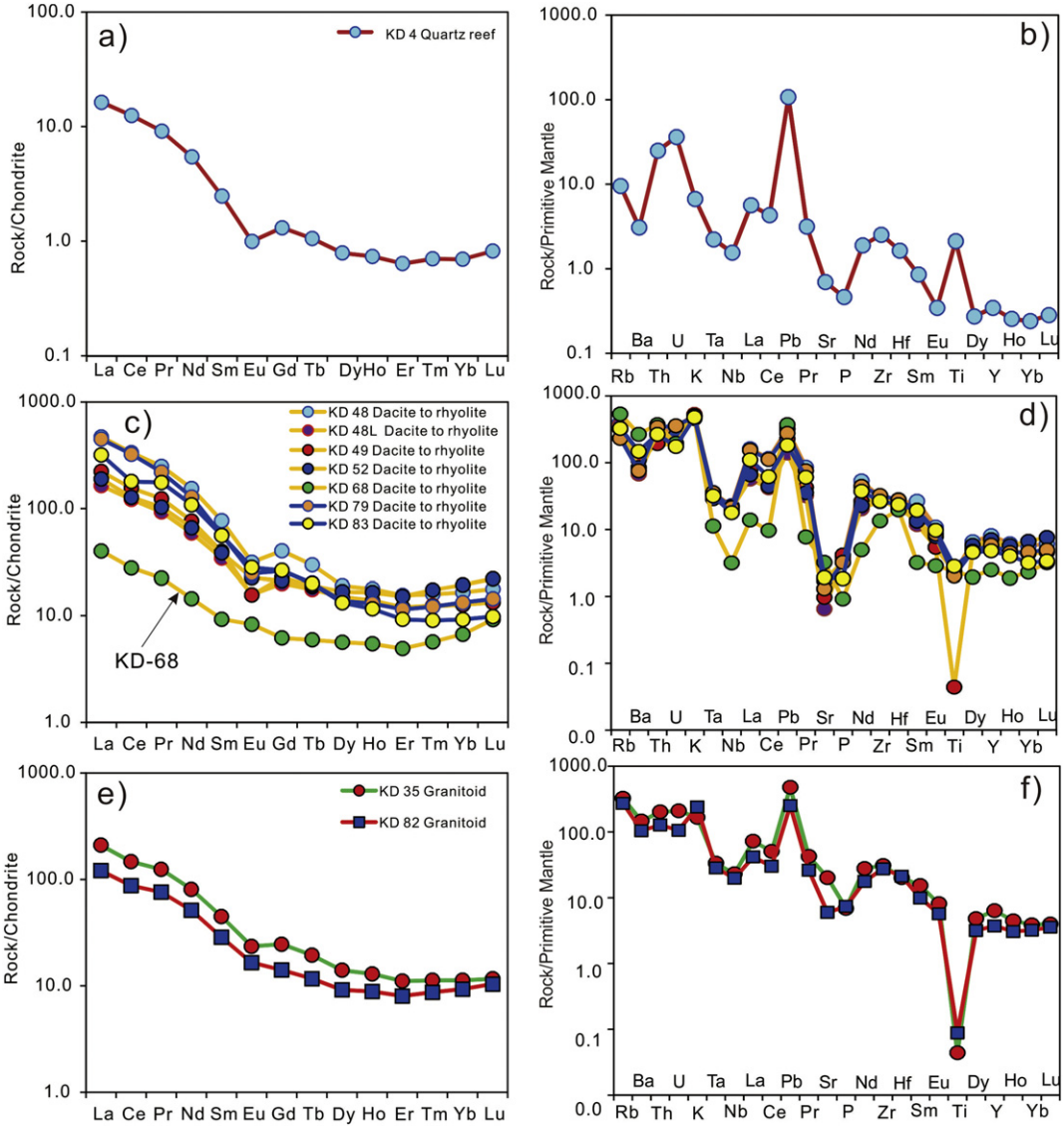


Fig. 4. Chondrite-normalized REE and primitive mantle-normalized trace element plots for the brecciated quartz reef (KD 4), dacite to rhyolite (KD 48, KD 48L, KD 49, KD 52, KD 68, KD 79, KD 83), granitoid (KD 35, KD 82) from the study area. Chondrite and primitive mantle values are from Sun and McDonough (1989).

housed at University of Kerala, India, and Michigan Technological University, USA, respectively.

3.3. Impact-related deformational features

Planar Fracture and ballen texture in quartz were studied using Carl Zeiss EVO 18 Secondary Electron Microscope equipped with CL detector, BSE, EDS and magnification of 5 to 300,000×, housed at Sophisticated Instrumentation and Computation Centre, University of Kerala, India.

The deformational features in zircon were studied with a FEI Philips XL 40 Environmental Scanning Electron Microscope (ESEM) at the Applied Chemical and Morphological Analysis Laboratory, Michigan Technological University, USA.

Reidite spectra were obtained by Laser Raman Spectroscopy using Jobin-Yvon LabRAM HR800 Raman Spectrometer where the wavelength of laser (He-Ne) is 632.8 nm, at Michigan Technological University, USA. The spectral range of the equipment is from 100 to 3600 cm^{-1} shift from the laser line, accomplished with an edge filter. The Raman system is fitted with XYZ mapping stage as well as confocal arrangement enabling imaging studies.

3.4. Zircon separation and analysis

Zircon separation from the crushed rocks was performed at the Yu'neng Geological and Mineral Separation Survey Centre, Langfang City, Hebei Province in China using a magnetic separator and density methods, followed by handpicking under a binocular microscope. The external morphology was studied using a binocular microscope under reflected light. The zircon grains were mounted onto an epoxy resin disk and then polished to expose the internal texture, and were examined under transmitted and reflected light. The internal zircon textures were studied using Cathode Luminescence (CL) images acquired on a scanning electron microscope (SEM) (JSM510) equipped with a Gatan CL probe at the Beijing Geoanalysis Centre.

Zircon U-Pb and trace element analyses were conducted using LA-ICP-MS at Wuhan Sample Solution Analytical Technology Co. Ltd. Detailed operating conditions for the laser ablation system and the ICP-MS instrument and data reduction are the same as those described by Liu et al. (2008, 2010). Laser sampling was performed using a GeoLas 2005. An Agilent 7700e ICP-MS instrument was used to acquire ion-signal intensities. Helium was applied as a carrier gas. Argon was used as the make-up gas and mixed with the carrier gas *via* a T-connector before entering the ICP. A "wire" signal smoothing device is included in this laser ablation system, by which smooth signals are produced even at very low laser repetition rates down to 1 Hz (Hu et al., 2012). Each analysis incorporated a background acquisition of approximately 20–30 s (gas blank) followed by 50 s of data acquisition from the sample. An in-house Excel-based software ICPMSDataCal (Ver. 10.0) was used to perform off-line selection and integration of background and analyte signals, and time-drift correction and quantitative calibration for U-Pb dating (Liu et al., 2008, 2010).

Zircon 91500 was used as external standard for U-Pb dating, and was analyzed twice every five analyses. Time-dependent drifts of U-Th-Pb isotopic ratios were corrected using a linear interpolation (with time) for every five analyses according to the variations of 91500 (Liu et al., 2010). The U-Th-Pb isotopic ratios used for 91500 are from Wiedenbeck et al. (1995). Concordia diagrams and weighted mean calculations were made using Isoplot/Ex_ver3 (Ludwig, 2003).

4. Results

4.1. Geochemistry of impactites

Chemical analyses were done for 15 samples, which includes one brecciated quartz reef, two granitoids, two brecciated granitoids, three

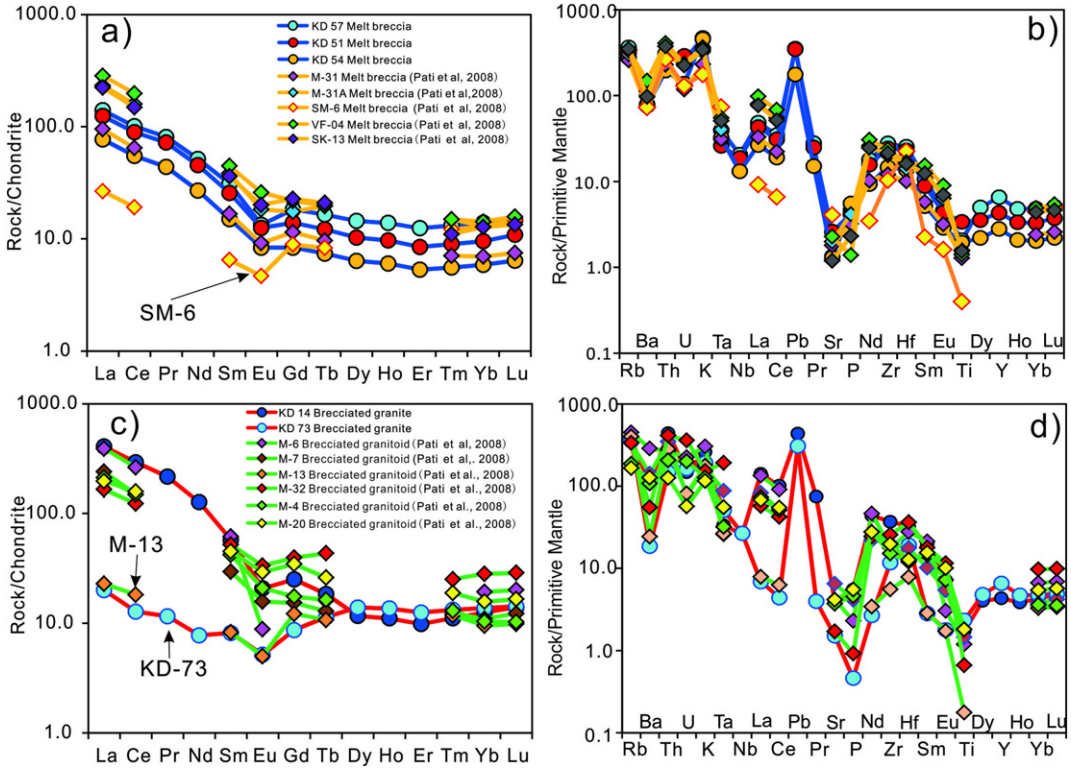


Fig. 5. Chondrite-normalized REE and primitive mantle-normalized trace element plots for the melt breccia (KD 57, KD 51, KD 54, M 31, M 31A, SM 6, VF 04, SK 13), brecciated granite (KD 14, KD 73) and vis-à-vis Pati et al. (2008).

melt breccias, and seven dacites to rhyolites. Our geochemical data were combined with those from 12 samples published by Pati et al. (2008) for a more comprehensive overview of the compositional variability among the different rock types at Dhala (Table 1).

4.1.1. Major elements

The rock types in the study area include granitoids, brecciated granitoids, melt breccia and dacite-rhyolite. Their major element compositional range shows ~65 wt% to nearly 80 wt% SiO_2. In general, the major elements show scatter compared to SiO_2 contents, with no apparent trends within any given rock type or among different rock types. The melt breccia samples from this study are geochemically more similar to the dacite-rhyolite than the granitoid target rocks as reflected in their Al_2O_3, Fe_2O_3, Na_2O, and K_2O contents. The dacite-rhyolite and melt breccia have extremely high alkali contents and depleted calcium relative to the crystalline granodiorite-granite and brecciated granite target rocks, and therefore do not reflect the primary composition of these rocks. Melt breccias from the Pati et al. (2008) study appear to be slightly different in major elements than those from the current study. All of the dacite-rhyolite and melt breccia are also depleted in MgO, and most in Fe_2O_3, at a given SiO_2 content relative to the granitoids and brecciated granitoids (Fig. 3).

4.1.2. Trace elements

Chondrite-normalized rare-earth element (REE) plots show generally similar patterns (Figs. 4 and 5). These silicic rocks are characteristically enriched in light rare-earth elements (LREE) with a slight negative Eu anomaly and slight depletion in middle rare-earth elements (MREE). However, clear differences are displayed in the case of a few elements. Four samples have anomalous trace element patterns in comparison to the other samples. The brecciated granitoid samples KD73 and M13 and melt breccia sample SM-6 are significantly depleted in LREE relative

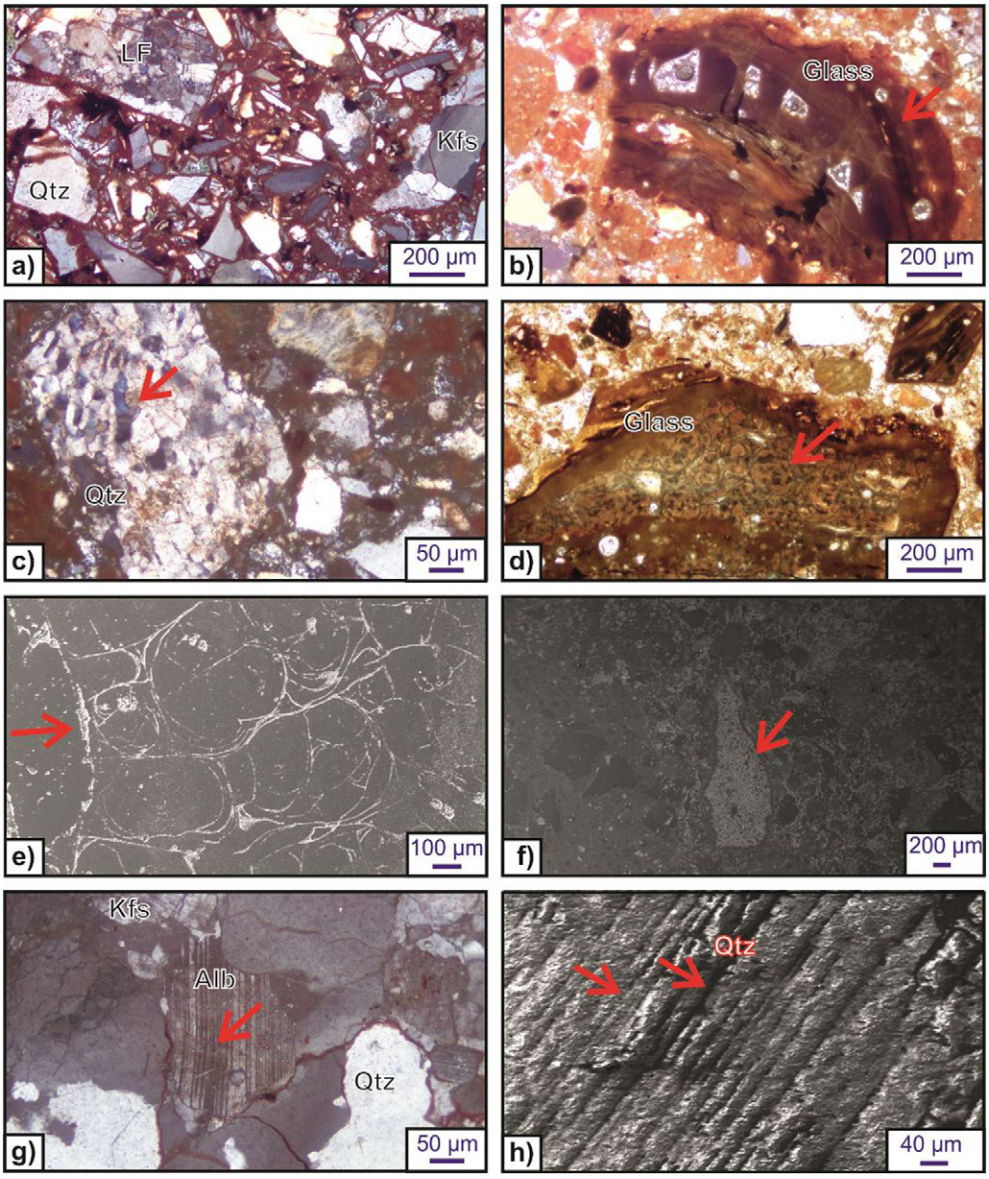


Fig. 6. Photomicrographs and SEM images of different lithounits of the study area (a) Brecciated granite showing angular clasts dominated by quartz (Qtz), K-feldspar (Kfs), lithic fragment (LR) and plagioclase (Alb) (probably albite) (b) Cumulates of glassy material, which is obvious in melt breccia containing fragments of rounded to sub-angular clasts. Notice the flow texture in the glassy part of the rock, evidence for melt movement (c) Unique ballen quartz developed due differential rate of polymorph conversion (d) Ballen quartz and flow texture in melt breccia. A cumulate shows banding parallel to outline indicating molten movement (e) SEM image of ballen quartz (f) Checkerboard feldspar giving a sieve appearance to feldspar (SEM image) (g) microfaults in plagioclase (probably albite due to closely spaced lamellae) (h) well developed planar fracture in quartz.

to the other samples, but have similar abundances and patterns in MREE to HREE. Dacite-rhyolite sample KD 68 is distinct from all other rock types with depletion in REE relative to the other samples and a slightly positive Eu anomaly. Chondrite-normalized REE and primitive mantle-normalized trace element plots, excluding the four anomalous samples, clearly show the overlapping range of compositions among both target granitoid and dacite-rhyolite rocks and the brecciated and/or melted impact rocks except for vertical shifts which point to a common parentage for all of them.

The compositional range of SiO_2 might correspond to crystal fractionation which at least partially explains the variability in trace element geochemistry. If we only consider the average for each rock type the trace element concentrations are broadly similar. The rocks including dacite to rhyolite, melt breccia and brecciated granitoid dominantly show negative Ba, Nb, Ta, Sr, P, Ti anomalies and positive K, Pb, Th anomalies. The brecciated quartz reefs show prominent negative Ba, Nb, Ta, Sr, P, Eu anomalies, and positive Th, U, Pb, Ti anomalies. The results in this study are similar to those reported by Pati et al. (2008) (Fig. 5a–d). The fact that the REE patterns are similar among all rock types, including the glassy, extremely high-K_2O rocks, that have clearly undergone hydrothermal alteration, attest to limited mobility of these elements during fluid-rock interaction. There is some scatter in major elements, but the overall similarity in trace elements show that these rocks were all likely derived from a similar source, under similar P-T-fO_2-H_2O conditions.

4.2. Impact-related deformational features and textures

4.2.1. Brecciation and melting

The impactites in Dhala, based on clast-matrix ratio, can be classified into a clast-rich unit represented by the brecciated granite; an equal clast-matrix proportion represented by the melt breccia, and a matrix-rich variety represented by the dacite to rhyolite rocks. Fig. 6a shows the representative photomicrograph of brecciated granite (KD 73) with randomly oriented angular clasts. The matrix has a dull appearance due to weathering although the clasts still maintain their angularity.

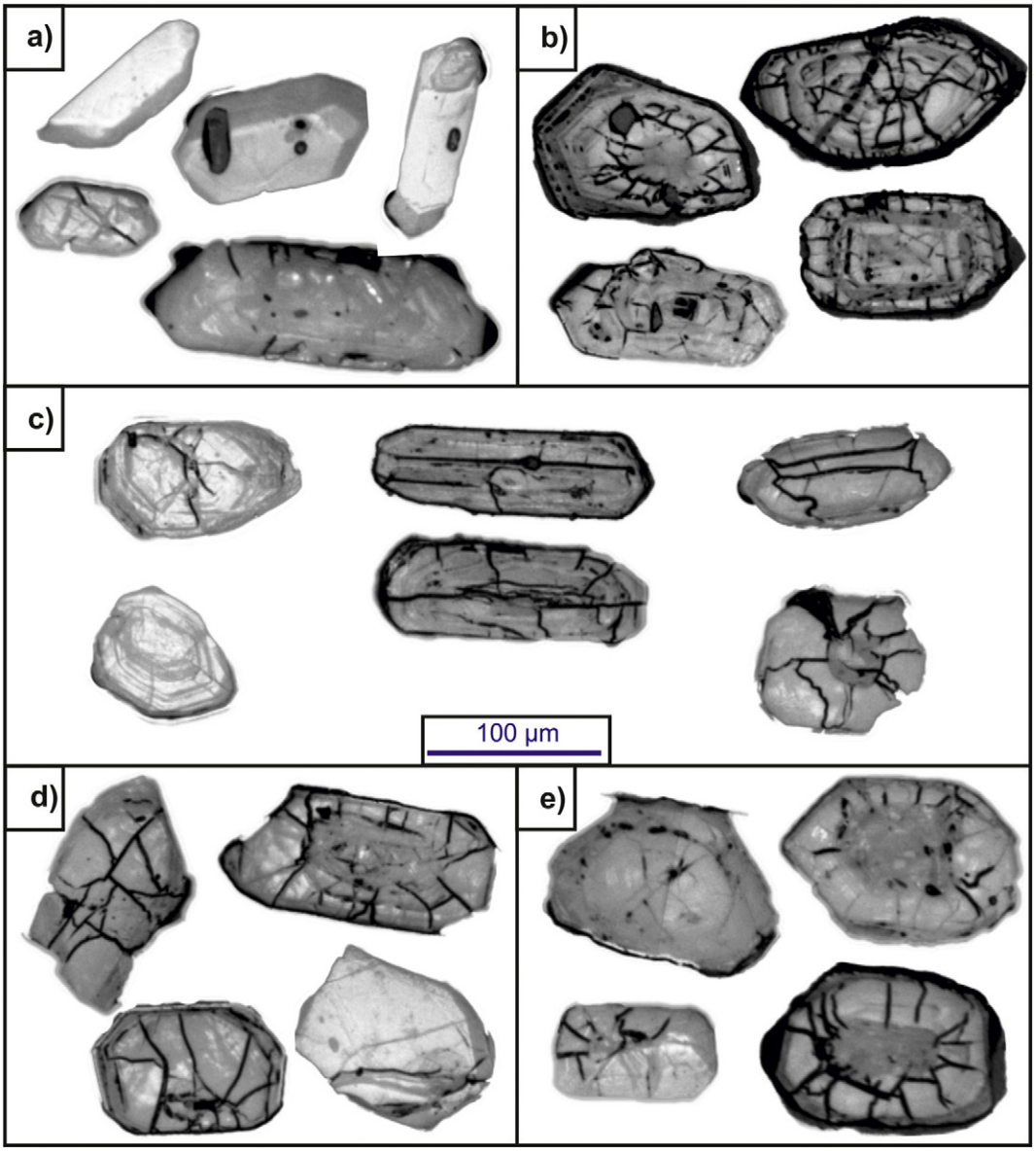


Fig. 7. Morphology exhibited by zircon grains under reflected light a) brecciated granite b) & c) melt breccia d) dacite to rhyolite e) quartz reef.

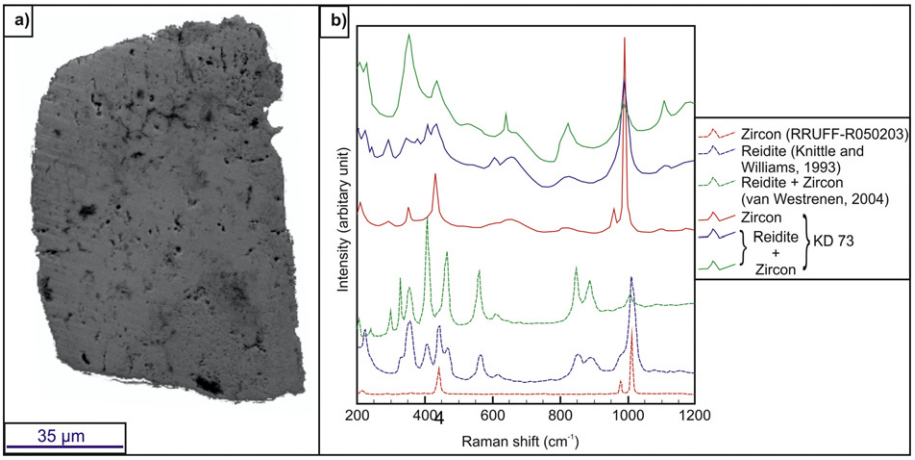


Fig. 8. (a) Reidite, a high pressure polymorph of zircon. Note the one directional planar fracture and absence of zoning (b) characteristic Raman spectra of zircon and reidite from KD 73.

Melting is often associated with impact which leads to the formation of melt rock and suevite. Melting in the Dhala rocks is mainly seen in melt breccia (KD 51, 57) where glassy material accumulates and often resembles pseudotachylite (Fig. 6b). The melt breccia along with dacite to rhyolite rock is products of melting of the target rock.

4.2.2. Ballen quartz

The ballen quartz has been reported from Dhala by Pati et al. (2008). These are spheroidal bodies which penetrate or abut each other (Ferrière et al., 2009). The formation of ballen is associated with the phase transition of quartz to its high P-T polymorphs. The characteristic feature of the ballen texture seen in the present study is the differential interference colour produced by different fish-scale like pattern of quartz (Fig. 6c), which might reflect a differential rate of polymorph conversion. Ballen is usually seen engulfed in a glassy melt (Fig. 6d), a feature readily seen in SEM image (Fig. 6e), and in the present study this is mainly seen in melt breccia.

4.2.3. Checkerboard feldspar

Checkerboard or sieve texture is an intragranular texture (e.g., Grieve, 1975; Reimold, 1982) formed in a thermally altered/shocked feldspar (Bischoff and Stöffler, 1984). Co-existence of checkerboard feldspar together with well-developed ballen structures in quartz is rare as these form under different impact pressures (Bischoff and

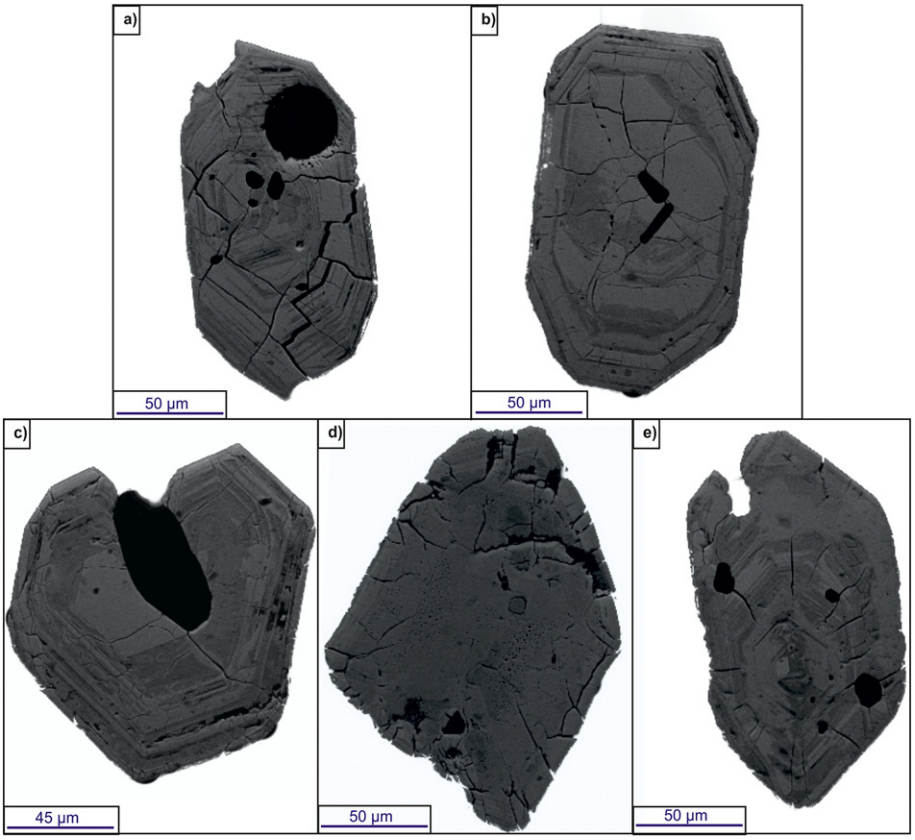


Fig. 9. Deformational features in zircon (a) PDF in zircon. The fractures are filled with glassy material (b) spider-net like pervasive cracks in a perfectly zoned zircon grain (c) cracks parallel to zoning, which usually forms one set of fractures in PDF (d) peripheral cracks indicating re-establishment of equilibrium in the core part (e) embedded fragments of host material.

Stöffler, 1984). Checkerboard feldspar is seen in the brecciated granite (KD 73) of Dhala area. The sieves in the checkerboard are well-developed in this rock (Fig. 6f) even though the rock is highly fractured.

4.2.4. Kinked feldspar

Kink bands can be formed either due to intracrystalline deformation or impact event. Kink bands have sharper and more planar boundaries (Blenkinsop, 2000). Kink exhibited by feldspar in the brecciated granite (KD 73) of the study area are manifested in the form of bending of twin lamellae and micro-faults (Fig. 6g). Such features are formed due to the consequences of deformation, which could be at relatively low pressures (Hirth and Tullis, 1994).

4.2.5. Flow texture

Flow texture of glassy material is a quite obvious feature in melt breccia (Fig. 6b, d) indicating melt movement. Such melt movement can be observed in Fig. 6d where flow bands approximately parallel the outline. The glassy material often accumulates and encloses fragments of rounded to sub-angular clasts. Some clasts are green in colour, probably due to chloritization. At places (Fig. 6d), the glassy margin is chilled with enclosing aphanitic melt clast, which was probably by quenching from a melt (Osinski and Spray, 2001).

4.2.6. Planar fracture and planar deformation feature in quartz

The presence of Planar Fracture (PF) is among the robust evidence for an impact origin. Planar Fractures are parallel sets of multiple planar cracks or cleavages. This is exhibited by quartz in the brecciated granite (Fig. 6h). Planar Deformation Features (PDF), on the other hand, consist of narrow planes of glassy material arranged in parallel sets and it can be penetrative through a whole grain or occur in parts of a grain, but do not cross grain boundaries, cracks, faults or fractures that were present before PDF formation (Hamers et al., 2016). These are seen in quartz grains of brecciated granite but are barely visible and hence not presented here.

4.3. Zircon analysis

4.3.1. Zircon morphology

Zircon grains from brecciated granite (KD 73) (Fig. 7a) are brownish or colorless, transparent to translucent. Their shapes range from euhedral to subhedral, and some grains have prismatic to stumpy morphology. The grains are relatively small and show a size range from 30 to 150 μm, with aspect ratios of 3:1–1:1. In reflected light, some grains show irregular homogenous domains of melting texture with a few cracks. Many grains show clear oscillatory zoning, whereas some show patchy or sector zoning.

Zircons from the melt breccia (KD 51) (Fig. 7b) are euhedral to subhedral with dark brownish colour. Most of them are prismatic, but a few display irregular shapes. Their lengths range from 80 to 200 μm, with aspect ratios of 2.5:1–1:1. Under reflected light, the grains from this sample also show abundant radiating cracks indicating an impact. Under CL, the grains generally show discontinuous oscillatory zoning. Zircons with weak irregular homogeneous domains are also common, with the original zircon growth zones cut by the low-U content domains, possibly representing melting and recrystallization. A few grains also show banded or patchy zoning. Minor, structureless grains are also present.

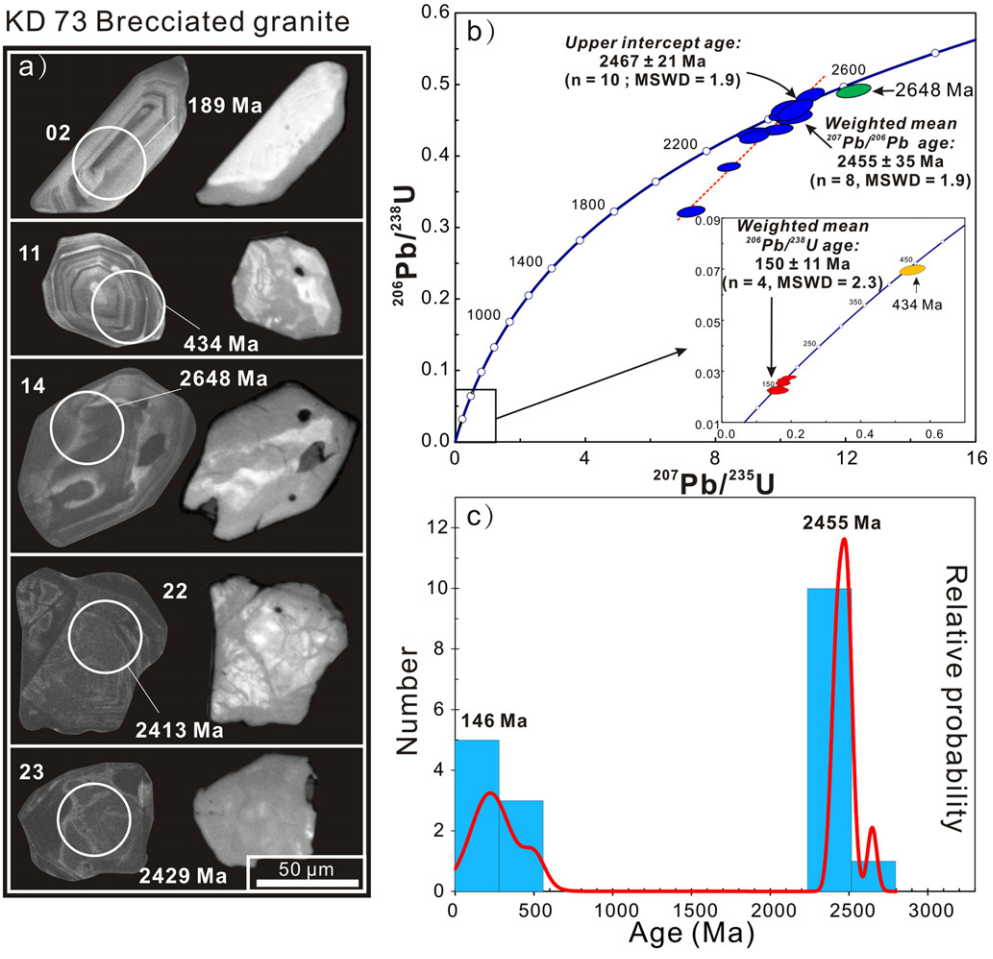


Fig. 10. Zircon analysis for KD 73 (brecciated granite) (a) spots analyzed (b) U-Pb concordia plots (c) age data histogram.

Most of the zircon grains from the other melt breccia sample (KD 57) are dark brownish, and some grains are colorless and transparent (Fig. 7c). Their shape ranges from euhedral to anhedral, with prismatic to stumpy morphology, and length ranging from 50 to 150 μm, with aspect ratios of 2.5:1–1:1. Most of the grains display homogeneous structures with the original growth zones interrupted by low-U content domains leading to a discontinuous texture. Some grains possess sector or patchy zoning. Under reflected light most grains show radiating cracks suggesting impact.

Zircons from sample KD 48 of rhyolite are dark brownish, euhedral to subhedral, and most of the grains show prismatic morphology. Their size ranges from 50 to 100 μm, with aspect ratios of 3:1–1:1 (Fig. 7d). Most of the grains display oscillatory zoning, and discontinuous growth zones, possibly due to magma mixing or kinetic effects. A few grains show banded zoning or sector zoning. Importantly, many grains in reflected light microscopy show the common presence of radiating cracks suggesting an impact affected them. They also show irregular spongy domains, suggesting recrystallization. Some grains are structureless with low-U content.

Zircons from sample KD 4 (giant quartz reef) are dark brownish, and a few grains are transparent, euhedral to anhedral. Their lengths range from 50 to 120 μm, with aspect ratios of 2:1–1:1 (Fig. 7e). The primary zircon growth zones are cut by melted zones with low-U content and homogeneous texture, suggesting recrystallization in a kinetic setting. A few grains display weak discontinuous oscillatory or patchy zoning. Minor low-U contents zircons are also common. Under reflected light microscopy, the grains show minor cracks.

4.3.2. Shocked zircon, PDF, cracks, and melting and quenching in zircon

In this study, we identified the high pressure polymorph of zircon, reidite, in the brecciated granite. Reidite is usually rare and considered as a diagnostic mineral in impact craters. It is usually denser than zircon, and hence is brighter in the BSE images (Fig. 8a). This high pressure polymorph is characterized by one set of planar fracture along the edges of the crystal. These fractures impart a lamellar appearance to reidite. The Raman spectrum of the zircon samples KD 73 (Fig. 8b) also shows the presence of reidite. The grains exhibit a typical spectra of zircon (correlated with RRUFF-R050203) as well as a combination of both zircon and reidite (e.g., Knittle and Williams, 1993; Van Westrenen et al., 2004). The spectrum of zircon shows a peak at 1008 cm^{-1} (anti-symmetric stretching of SiO_4 group) and 974 cm^{-1} (symmetric stretching of Si—O) (Dawson et al., 1971). The other peaks are in a low-frequency region, whereas reidite shows more peaks due to its lower crystal symmetry (Gucsik et al., 2004b). The persistence of peaks at 974 and 1008 cm^{-1} in reidite are from the remaining untransformed zircons (Van Westrenen et al., 2004; Gucsik et al., 2004b).

PDFs in zircon are reported from several ancient and large impact structures (e.g., Leroux et al., 1994; Huffman and Reimold, 1996). PDF (Fig. 9a) in zircons of Dhala are mainly detected from melt breccia (KD 51) though such features are suspected in other litho-units. The haphazard cracking, melting and quenching make it difficult to identify PDF in zircons of other litho-units. Two sets of fractures are visible and these often coincide with the zoning pattern. These fractures are filled with glassy material and in places exhibit en echelon fractures (Fig. 9a).

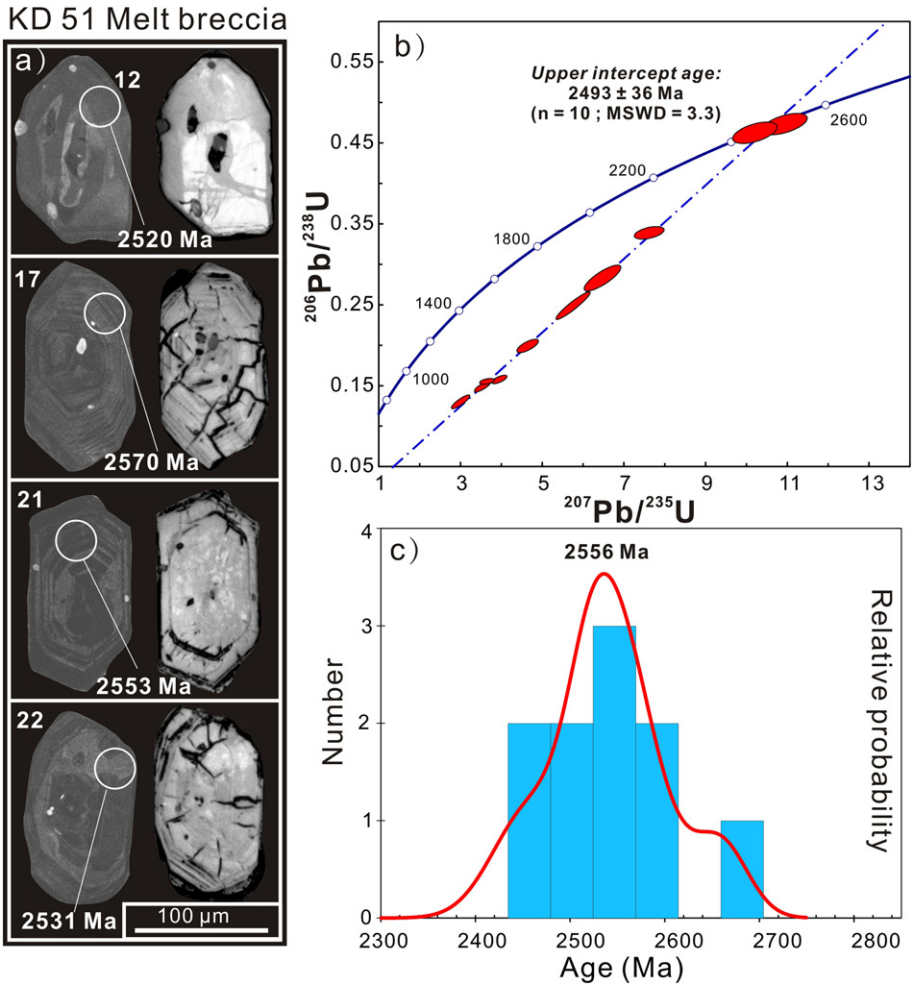


Fig. 11. Zircon analysis for KD 51 (melt breccia) (a) spots analyzed (b) U-Pb concordia plots (c) age data histogram.

The BSE images of zircons, both in rhyolite and melt breccia, show that almost all crystals possess pervasive cracks giving an overall spider-net like appearance to the zoned crystal (Fig. 9b). The individual cross-cutting relationship of the crystal zoning and radial fracture indicates that the fracturing is impact related. In some crystals, the cracks are present only along the periphery (Fig. 9c, d), and is absent in the core zone. This may be because of the healing established at the core. Extremely fine microplanes are rare in these crystals, though confirming their presence requires specialized, extremely high-resolution instrumentation.

The zircon grains separated from the undeformed clasts in brecciated granite are notably free from such cracking and subsequent filling. Melting and quenching are noted in almost all zircon grains in the dacite to rhyolite and melt breccia (Fig. 9a–e). Quenching has caused the deposition of the melted material within the fractures. The opaque portion of the cracks may be formed from the melt (glassy material) of host crystal or from a foreign source or due to the presence of excessive mounting medium. Embedded fragments of the host material are found in some of the crystals (Fig. 9e). Plastic deformation is virtually absent in the crystals indicating that the fractures present are a manifestation of shock induced shear stress alone.

4.3.3. Zircon U-Pb geochronology and Pb loss

Representative CL images of zircon grains from the four samples dated in this study are given in Figs. 10–14, and the data are plotted in concordia diagrams together with age data histograms. The U-Pb analytical data are given in Appendix C (supplementary material). The concordance values were computed using the equation (Bracciali et al., 2013; Horstwood et al., 2016; Spencer et al., 2016):

$$\text{Concordance}\ (\%) : 100 \times \left(^{206}\text{Pb}/^{238}\text{U age}\right)/\left(^{207}\text{Pb}/^{206}\text{Pb age}\right)$$

In general, the oldest group of xenocrystic zircons (see below) has low concordance, obviously due to Pb loss from the subsequent thermal event(s). If zircon grains have undergone Pb-loss, they often do not show high concordance, and in such cases, the common practice is that the individual spot age concordance is not used, but the main focus would be on the uncertainties of the discordia to define the quality of age data.

A brief description of the zircon characteristics and age results in individual samples are presented below.

4.3.3.1. Sample KD 73 (brecciated granite). A total of nineteen zircon spots were analyzed from sample KD 73 (Fig. 10a), and the data can be divided into four groups. The oldest zircon in this sample has a $^{207}Pb/^{206}Pb$ age of 2648 ± 57 Ma, and Th, U contents are 303 ppm and 174 ppm, with Th/U ratio of 1.74. Therefore, this zircon is considered as a xenocryst probably captured from the basement during magma emplacement. Ten spots fall along a discordia and yield upper intercept age of 2467 ± 21 Ma (MSWD = 1.9, n = 10) with weighted mean $^{207}Pb/^{206}Pb$ age of 2455 ± 35 Ma (MSWD = 1.9, n = 8) (Fig. 10b). The age data histograms are shown in Fig. 10c. The grains show Th contents from 168 to 1444 ppm and U contents from 189 to 826 ppm, with

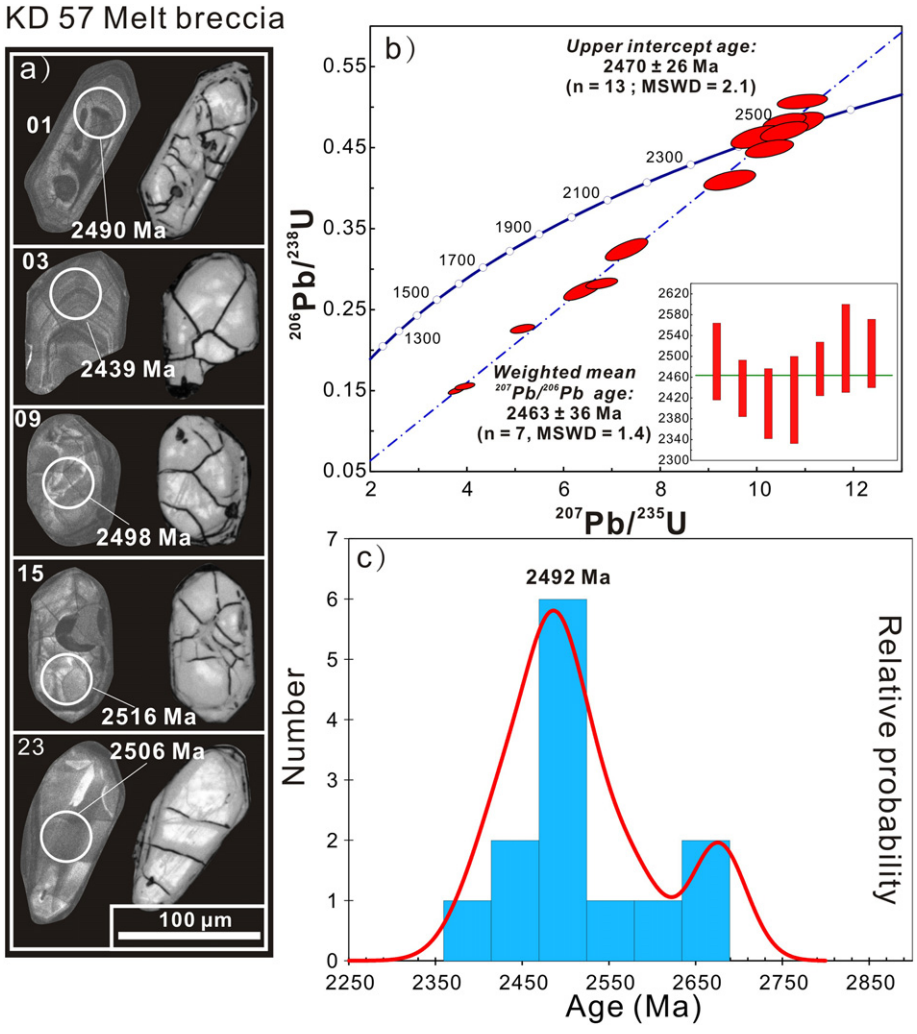


Fig. 12. Zircon analysis for KD 57 (melt breccia) (a) spots analyzed (b) U-Pb concordia plots (c) age data histogram.

Th/U ratios from 0.43 to 2.45. One spot shows a very young $^{206}Pb/^{238}U$ age of 434 ± 10 Ma, with Th, U contents of 225 ppm and 275 ppm and Th/U ratio of 0.82. The last group has seven zircon spots yielding an upper intercept age of 150 ± 11 Ma (MSWD = 2.3, n = 4). They show Th contents of 236–469 ppm and U contents of 373–576 ppm, with Th/U ratios of 0.54–0.96. We interpret the data to suggest magmatic crystallization at ca. 2.46 Ga.

4.3.3.2. Sample KD 51 (melt breccia). Ten zircon spots were analyzed from this sample (Fig. 11a) and the results yield an upper intercept age of 2493 ± 36 Ma (MSWD = 3.3, n = 10) (Fig. 11b). The age data histograms are shown in Fig. 11c. The Th contents are 124–1880 ppm, U contents show a wide range from 155 to 1616 ppm, with high Th/U ratios ranging from 0.63 to 1.81, mostly representing magmatic zircons. The data indicate magmatic crystallization at ca. 2.5 Ga. Apart from two concordant zircon grains, the other data fall along a single discordia, suggesting Pb loss from a subsequent short-lived thermal event, as growth of new concordant zircon grains is not seen.

4.3.3.3. Sample KD 57 (melt breccia). A total of thirteen zircon spots (Fig. 12a) were analyzed and the data define an upper intercept $^{207}Pb/^{206}Pb$ age of 2470 ± 26 Ma (MSWD = 2.1, n = 13) with weighted mean $^{207}Pb/^{206}Pb$ age of 2463 ± 36 Ma (MSWD = 1.4, n = 7) (Fig. 12b). The age data histograms are shown in Fig. 12c. The Th, U contents show a range of 122–1027 ppm and 130–908 ppm, with Th/U ratios range from 0.62 to 3.31, suggesting they are magmatic zircons. The data clearly indicate magmatic crystallization at ca. 2.47 Ga followed by Pb loss during a subsequent thermal event, which did not lead to the crystallization of concordant zircons.

4.3.3.4. Sample KD 48 (dacite to rhyolite). A total of seventeen zircon spots were analyzed from sample KD 48 (Fig. 13a), and the results can be divided into two groups. One group defines a discordia with upper intercept age at 2499 ± 27 Ma (MSWD = 2.9, *n* = 15), with weighted mean $^{207}Pb/^{206}Pb$ age of 2482 ± 40 Ma (MSWD = 1.7, *n* = 6) (Fig. 13b). The age data histograms are also shown in Fig. 13c. The zircon grains show Th content of 85.6–1114 ppm and U content of 71.4–1139 ppm, with Th/U ratios range from 0.47–1.90. Two spots yield $^{207}Pb/^{206}Pb$ age of 2383 ± 69 Ma, 2366 ± 67 Ma. Their Th content are 102 ppm and 167 ppm, U content are 104 ppm and 186 ppm, with Th and U ratios are 0.98 and 0.90, respectively. We interpret the results to indicate magmatic crystallization of this rock at ca. 2.5 Ga, followed by a subsequent event of prominent Pb loss. The absence of concordant zircon data for this later event would suggest that the thermal event was short-lived without sufficient time for new grains to crystallize.

4.3.3.5. Sample KD 4 (quartz reef). Twenty-three zircon spots were analyzed from sample KD 4 (Fig. 14a), which can be divided into three groups. One group of nine zircon spots show $^{207}Pb/^{206}Pb$ age range of 2772–2550 Ma with seven spots defining an upper intercept age at 2679 ± 140 Ma (MSWD = 0.89, n = 7). Their Th, U contents are 397–843 ppm and 641–1154 ppm, with Th/U ratios of 0.58–1.15. Eleven zircon spots yield $^{207}Pb/^{206}Pb$ age range from 2483 to 2235 Ma with six spots defining an upper intercept age at 2443 ± 93 Ma (MSWD = 0.42,

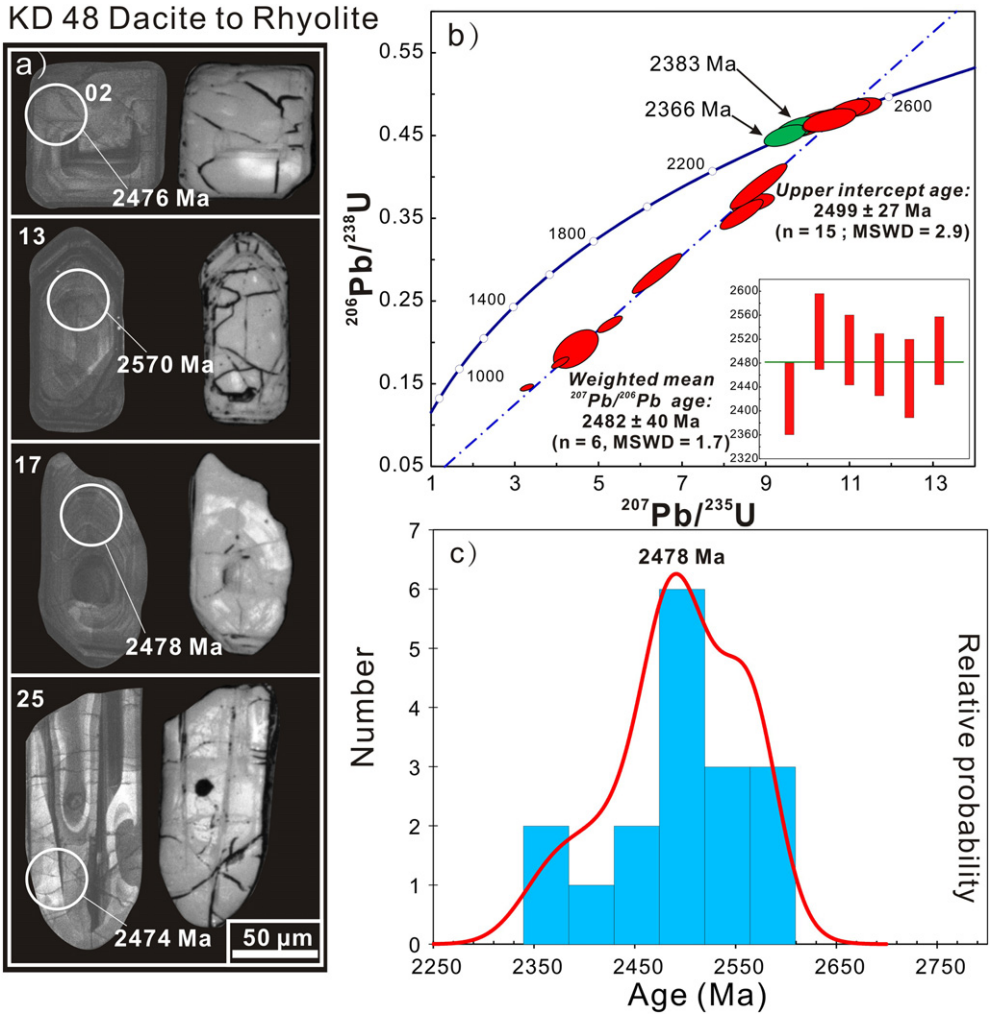


Fig. 13. Zircon analysis for KD 48 (dacite to rhyolite) (a) spots analyzed (b) U-Pb concordia plots (c) age data histogram.

n = 6) (Fig. 14b) and age histogram are shown in Fig. 14c. Their Th, U contents show a variety of 175–1936 ppm, 400–2382 ppm, with Th, U ratios of 0.35–3.57. Two spots show $^{207}Pb/^{206}Pb$ age of 1826 ± 97 Ma and 1767 ± 100 Ma, and their Th contents are 60.4 ppm and 194 ppm, U contents are 188 ppm and 985 ppm, with Th/U contents are 0.32–0.20. One spots shows $^{206}Pb/^{238}U$ age of 317 ± 5 Ma and Th, U contents are 185 ppm, 465 ppm, with Th/U ratios of 0.40.

4.3.4. Zircon REE

Rare earth element data on zircon grains from the samples in this study are given in Table 2.

Zircon grains from sample KD 73 can be divided into two groups based on their ages: i) Neoarchean to early Paleoproterozoic (2648–2392 Ma) and ii) Jurassic (ca.150 Ma). Both groups are characterized by LREE depletion, strong positive Ce anomaly and negative Eu anomaly (Fig. 15a–e). The Jurassic group shows relatively low LREE with a steep LREE to HREE pattern. Their La contents (0–0.58 ppm), together with higher $(Sm/La)_N$ values from 3.36 to 240.48, and Ce/Ce* from 65.36 to 1890.64 are similar to those of magmatic zircon grains (Hoskin, 2005). In contrast, the Neoarchean to early Paleoproterozoic group shows a relatively flat LREE pattern with high La contents (0.15–13.31 ppm), low $(Sm/La)_N$ (2.99–50.76) and Ce/Ce*(10.83–120.34) values, and their REE characteristics are broadly similar to those of hydrothermal zircon (Hoskin, 2005; Long et al., 2012). In general, hydrothermal zircon growth occurs in peralkaline environments (Corfu et al., 2003; Rubin et al., 1989), which is also supported by the high K_2O concentration in our sample. A correspondence between increasing LREE content with discordance of the zircon ages is also noted.

Zircon grains in sample KD 51 display an elevated REE pattern, positive Ce anomaly, negative Eu anomaly, and slight LREE depletion (Table 2). Compared with those in KD 73, the grains show higher REE contents in the range of 263–7265 ppm. Zircon from this sample displays higher La contents (0.15–83.07 ppm), low $(Sm/La)_N$ (2.94–18.17) and Ce/Ce*(5.59–59.04) values. The increase in LREE correlates with higher age discordance as well as the presence of distinct fractures in the grains, typical of zircon grains that have undergone dissolution and reprecipitation from aqueous fluids.

Zircon grains from sample KD 57 display an elevated REE pattern, positive Ce anomaly, negative Eu anomaly, and slight LREE depletion. The REE contents show a range from 431 to 3349 ppm. Most of the zircon from this sample display variable La contents (0.95–24.08 ppm), low $(Sm/La)_N$ (0.14–38.26) and Ce/Ce*(13.22–89.41) values, characteristic of hydrothermal zircons. However, two grains show low La contents (0.01 ppm, 0.03 ppm), high $(Sm/La)_N$ (961.84, 289.35), Ce/Ce* (1136.14, 437.18) values, indicating their unaltered nature. The difference between these two grains and the hydrothermal grains is also reflected in the absence of impact fracturing. A correspondence between increasing zircon LREE and age discordance is also evident.

Zircon grains from sample KD 48 show an elevated REE pattern, positive Ce anomaly, negative Eu anomaly, and a slight LREE depletion. The total REE contents show a range from 264 to 5727 ppm. They show high La contents (0.19–53.75 ppm), low $(Sm/La)_N$ (1.55–32.40) and Ce/Ce* (10.67–176.91) values. Two grains show low La contents (0.02 ppm, 0.05 ppm), high $(Sm/La)_N$ (777.86, 128.29), Ce/Ce* (502.1, 504.05) values, preserving the unaltered composition and lack of fracturing. The highly fractured zircon grains show high LREE contents, and the increase in LREE is reflected in the increasing age discordance.

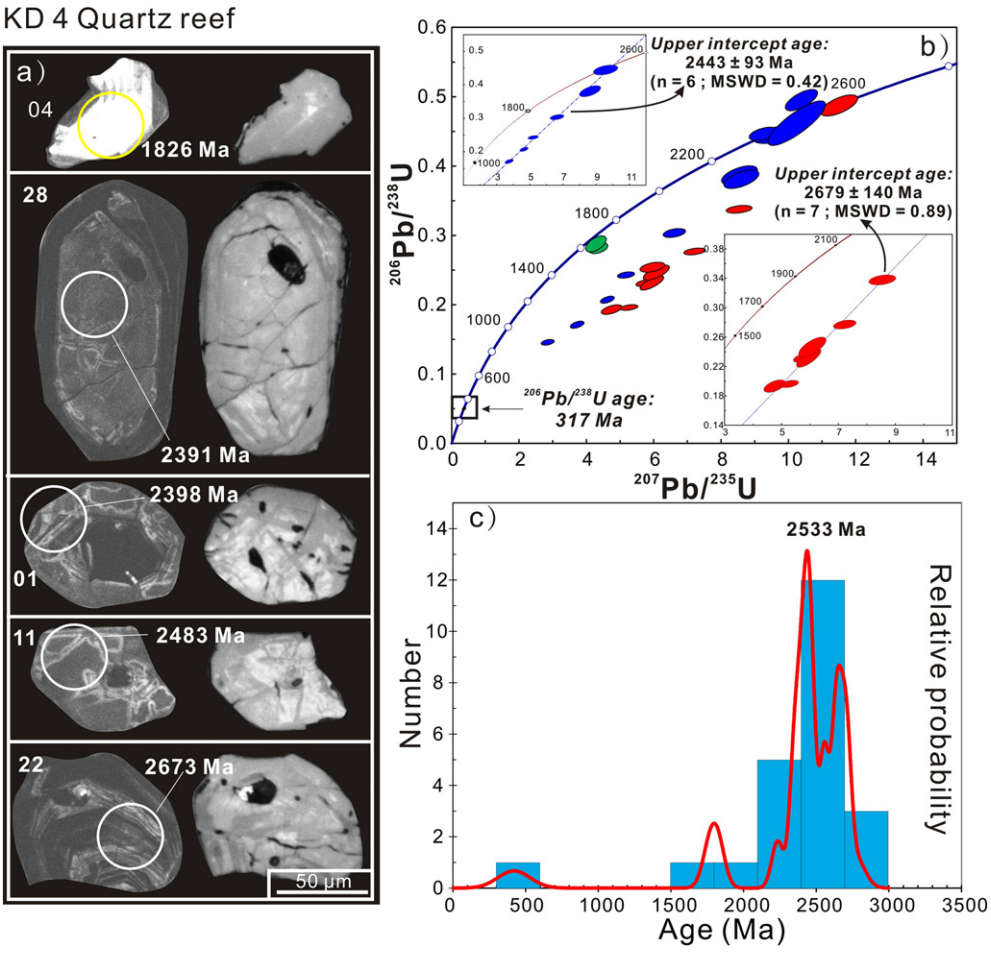


Fig. 14. Zircon analysis for KD 4 (quartz reef) (a) spots analyzed (b) U-Pb concordia plots (c) age data histogram.

Table 2
LA-ICP-MS zircon trace element data.

Spots no.	Element (ppm)														ΣREE	Ratio	
	La	Ce	Pr	Nd	Sm	Eu	Gd	Tb	Dy	Ho	Er	Tm	Yb	Lu		Ce/Ce*	(Sm/La)N
KD 73-02	0.02	20.81	0.05	1.37	3.64	1.23	16.24	4.15	43.30	16.21	74.09	16.35	167.48	38.11	403	636.22	240.48
KD 73-03	0.02	47.26	0.25	4.57	11.27	4.13	43.42	11.02	108.96	33.11	130.83	26.86	249.25	49.68	721	724.89	1043.99
KD 73-04	0.40	27.62	0.21	1.20	3.62	1.71	17.34	5.23	52.35	18.59	83.73	20.34	192.93	43.70	469	95.84	13.91
KD 73-06	0.04	33.72	0.09	2.07	3.04	1.56	13.31	3.73	38.12	13.02	57.83	13.89	134.26	30.21	345	530.29	108.61
KD 73-07	0.06	21.10	0.08	1.73	3.83	1.91	14.50	4.18	39.15	12.86	59.93	13.16	136.98	29.62	339	311.47	107.51
KD 73-11	0.08	27.58	0.15	2.04	2.98	1.33	18.84	6.21	76.58	31.09	151.13	36.10	373.65	78.32	806	252.73	56.64
KD 73-15	0.00	24.25	0.12	1.31	2.75	1.42	14.93	4.27	44.42	15.75	72.38	16.06	162.50	37.22	397	1890.64	3072.14
KD 73-17	0.58	17.08	0.12	1.08	1.26	0.74	6.55	2.02	22.74	8.67	41.14	10.47	110.64	28.23	251	65.36	3.36
KD 73-12	12.17	83.19	4.74	23.04	23.44	5.75	65.33	20.43	186.35	57.38	231.44	46.96	444.49	74.62	1279	10.95	2.99
KD 73-13	0.39	37.37	0.76	8.39	9.03	2.66	33.72	9.46	94.65	30.78	120.85	24.77	213.72	38.43	625	68.57	35.95
KD 73-14	0.40	38.51	0.69	7.79	10.49	2.61	45.01	12.12	126.98	41.47	168.12	33.26	292.86	50.93	831	73.75	41.09
KD 73-18	0.41	38.71	0.34	2.56	3.23	0.92	14.97	4.70	50.71	17.41	74.38	16.45	151.43	27.95	404	103.01	12.18
KD 73-19	2.67	86.54	3.70	28.07	36.22	8.52	143.28	42.18	407.03	127.16	502.12	97.75	792.40	141.83	2419	27.54	21.04
KD 73-20	13.31	110.62	7.64	44.22	31.65	9.56	86.93	24.09	215.33	63.96	240.75	49.36	440.32	76.27	1414	10.97	3.68
KD 73-21	1.78	86.97	2.50	15.99	15.85	4.95	52.94	14.90	133.24	36.32	135.12	27.95	249.05	40.71	818	41.27	13.80
KD 73-22	2.28	39.57	2.33	17.41	19.15	5.12	62.64	19.87	201.83	67.16	288.02	64.81	632.61	107.42	1530	17.15	13.01
KD 73-23	1.81	36.95	1.50	10.33	11.64	3.31	39.60	12.56	126.45	41.93	177.24	40.94	386.90	66.40	958	22.43	9.98
KD 73-24	6.76	78.70	7.81	51.56	46.01	10.09	109.32	30.28	276.42	80.90	319.94	68.87	649.46	102.55	1839	10.83	10.54
KD 73-25	0.14	21.88	0.23	2.41	4.75	0.87	22.02	7.49	95.21	36.04	166.32	38.24	372.18	68.12	836	120.34	50.76
KD 51-06	25.36	259.91	34.82	203.56	144.57	43.24	261.73	62.42	451.68	100.80	322.08	59.47	526.78	70.09	2567	8.75	8.83
KD 51-07	14.75	172.30	21.34	135.11	89.43	26.59	188.35	44.59	336.76	77.88	247.16	43.73	361.96	54.82	1815	9.71	9.39
KD 51-12	3.69	38.50	3.64	23.13	16.86	5.63	41.76	10.26	95.63	27.36	113.21	23.60	229.98	45.30	679	10.52	7.08
KD 51-15	0.15	11.07	0.23	2.55	1.78	0.93	8.54	2.32	24.80	9.02	44.37	11.63	121.25	24.38	263	59.04	18.17
KD 51-16	9.58	107.58	11.68	68.40	51.52	15.89	114.01	27.76	234.97	59.85	210.71	40.37	355.87	57.20	1365	10.17	8.33
KD 51-17	80.14	594.67	67.46	401.65	251.92	77.35	494.87	111.59	790.21	172.67	528.59	93.00	755.79	117.10	4537	8.09	4.87
KD 51-19	83.07	1843.68	90.20	516.32	328.11	103.45	690.83	162.35	1163.76	251.07	746.73	126.45	1016.64	142.01	7265	21.30	6.12
KD 51-20	12.69	176.79	17.16	109.07	68.07	21.10	130.49	27.49	182.38	42.56	135.68	25.03	214.24	34.52	1197	11.98	8.31
KD 51-21	58.86	239.83	31.25	163.55	111.59	39.84	246.73	60.36	465.91	113.73	391.59	76.57	664.43	100.13	2764	5.59	2.94
KD 51-22	73.53	528.79	63.96	388.44	261.40	81.95	542.32	131.50	989.57	220.85	685.56	119.98	943.90	129.43	5161	7.71	5.51
KD 57-01	2.68	61.05	1.69	12.12	9.67	3.11	24.66	6.80	65.83	20.19	86.24	17.88	151.79	26.96	491	28.70	5.59
KD 57-03	0.14	18.27	0.31	2.45	3.38	0.71	14.25	4.63	55.44	19.94	90.44	19.91	192.66	33.47	456	89.41	38.26
KD 57-05	0.95	34.61	1.40	9.30	8.11	2.71	26.64	7.67	75.28	25.11	100.05	21.78	200.51	35.92	550	30.00	13.18
KD 57-06	0.01	55.68	0.23	3.89	6.56	1.85	23.65	7.12	69.77	22.28	86.50	18.87	170.68	26.38	493	1136.14	961.84
KD 57-07	22.80	392.58	35.12	220.32	156.03	44.40	297.93	70.45	524.11	125.01	401.16	72.69	588.31	85.07	3036	13.87	10.60
KD 57-08	5.56	99.19	10.13	70.11	50.40	12.67	113.98	28.21	248.64	69.91	254.57	49.08	404.41	68.29	1485	13.22	14.03
KD 57-09	5.57	127.49	9.31	60.29	46.25	13.00	105.54	23.97	195.01	49.37	171.93	31.93	260.40	40.66	1141	17.70	12.85
KD 57-10	10.61	234.20	15.91	104.56	76.69	21.20	156.14	38.37	306.85	82.69	297.97	57.86	493.40	79.58	1976	18.03	11.20
KD 57-12	0.03	36.63	0.24	3.55	5.54	1.13	22.21	6.49	65.64	21.69	91.69	19.03	176.49	30.34	481	437.18	289.35
KD 57-15	1.44	51.81	2.55	16.38	11.13	2.76	22.89	6.90	57.82	16.96	66.60	14.39	136.42	23.21	431	27.10	12.01
KD 57-18	10.92	178.26	13.88	89.74	72.78	17.93	131.64	30.52	236.75	59.08	193.11	37.53	293.27	43.27	1409	14.48	10.33
KD 57-20	24.80	501.37	39.23	244.28	180.66	49.94	313.41	74.69	575.77	128.66	421.44	75.63	631.39	87.65	3349	16.07	11.28
KD 57-23	2.01	54.57	3.82	28.86	26.52	6.85	93.77	22.27	212.55	61.49	229.38	42.52	346.11	54.94	1186	19.70	20.46
KD 48-03	0.19	37.28	0.24	2.72	3.89	0.88	15.47	4.83	49.65	17.29	72.47	15.64	146.66	25.75	393	176.91	32.40
KD 48-04	0.02	33.36	0.29	4.93	7.61	1.95	24.14	7.17	65.50	21.82	85.93	17.83	165.72	27.37	464	502.10	777.86
KD 48-05	0.51	77.52	0.96	6.17	6.39	1.73	25.82	7.14	69.83	23.35	94.32	19.88	175.72	29.94	539	111.06	19.59
KD 48-10	0.19	22.03	0.29	3.24	3.09	0.88	10.99	3.53	36.25	11.76	48.48	10.47	95.83	16.65	264	93.27	24.61
KD 48-15	0.45	32.28	0.58	4.96	4.32	1.07	10.92	3.19	34.10	10.65	44.82	10.25	105.39	18.50	281	63.10	14.74
KD 48-17	0.85	35.01	1.01	6.55	6.70	1.67	23.34	7.31	76.25	25.48	109.33	23.08	211.89	37.26	566	37.66	12.20
KD 48-18	0.05	41.08	0.13	3.00	4.15	1.35	21.13	5.79	56.27	18.45	74.80	15.76	137.74	23.54	403	504.05	128.29
KD 48-25	6.26	42.29	1.98	12.10	6.26	2.43	13.18	3.81	35.97	11.24	46.43	9.32	82.00	14.58	288	12.01	1.55
KD 48-02	11.92	458.57	15.24	92.34	65.60	19.90	139.74	37.78	287.59	71.43	229.59	39.88	323.80	48.22	1842	34.03	8.53
KD 48-08	53.75	529.25	35.55	215.23	136.05	44.99	296.51	73.06	572.85	133.04	420.24	69.90	553.19	77.05	3211	12.11	3.92
KD 48-11	2.42	116.66	3.31	23.67	23.51	6.53	72.65	19.43	165.63	48.49	173.85	32.02	258.19	43.48	990	41.25	15.07
KD 48-13	11.49	307.12	12.01	73.30	54.12	16.86	117.71	30.65	254.97	64.08	218.32	39.35	333.94	50.99	1585	26.15	7.30
KD 48-16	3.22	134.93	4.93	33.15	30.25	9.62	84.84	22.14	197.63	56.26	201.48	37.63	313.53	50.55	1180	33.89	14.56
KD 48-19	38.95	1795.16	47.52	282.26	199.15	61.55	429.88	106.04	818.13	198.50	633.81	108.09	875.18	133.08	5727	41.72	7.92
KD 48-21	12.98	283.06	17.10	103.89	81.78	25.59	201.41	56.31	483.26	127.98	433.03	79.87	650.55	99.22	2656	19.00	9.76
KD 48-23	31.04	610.93	29.12	167.83	113.59	37.29	235.14	58.42	470.45	109.19	351.14	61.19	507.52	74.26	2857	20.32	5.67
KD 48-24	51.13	381.58	25.02	142.74	88.47	28.21	183.12	45.82	358.35	83.34	262.31	46.74	365.77	54.18	2117	10.67	2.68
KD 4-01	6.72	49.27	5.39	31.03	20.81	6.23	53.47	15.02	133.95	41.62	178.80	34.74	341.68	67.18	986	8.19	4.80
KD 4-02	30.78	229.97	22.04	121.47	85.35	26.64	186.88	44.65	385.47	107.21	371.66	70.00	587.76	92.59	2362	8.83	4.29
KD 4-03	18.49	143.74	15.21	84.30	61.79	22.06	156.36	40.13	334.38	92.82	342.87	64.73	578.96	103.86	2060	8.57	5.18
KD 4-05	24.94	226.34	23.77	139.57	85.55	25.27	199.25	47.50	364.75	89.30	297.94	55.43	442.14	70.74	2092	9.30	5.31
KD 4-06	18.00	83.74	8.71	48.65	32.33	10.01	80.70	21.22	196.99	63.85	266.84	59.17	551.72	100.30	1542	6.69	2.78
KD 4-07	12.41	50.04	5.26	28.90	22.50	6.23	65.87	18.54	205.59	68.64	297.87	67.72	653.45	115.56	1619	6.19	2.81
KD 4-08	5.81	51.77	4.10	24.21	20.61	6.54	62.08	16.61	164.31	53.44	222.49	48.52	461.97	81.57	1224	10.60	5.49
KD 4-09	10.95	29.86	2.06	11.51	9.39	2.51	39.55	11.79	127.65	46.97	220.09	48.54	490.97	81.53	1133	6.30	1.33
KD 4-10	11.07	93.98	7.83	44.95	37.97	11.74	96.37	25.94	234.58	72.16	302.28	65.13	614.53	107.27	1726	10.09	5.31
KD 4-11	11.20	108.30	11.30	74.62	51.17	18.20	137.81	30.45	245.99	73.16	269.23	51.72	459.75	83.02	1626	9.63	7.08
KD 4-14	0.06	6.06	0.03	0.87	1.55	0.64	16.12	5.84	80.02	34.88	174.55	46.20	514.09	104.55	985	147.71	38.84
KD 4-16	5.95	59.62	4.82	32.67	21.77	4.49	71.22	18.93	205.57	72.37	305.57	67.00	637.09	107.80	1615	11.13	5.66
KD 4-18	50.83	197.19	39.96	247.31	169.11	35.34	317.74	70.06	547.60	144.85	476.41	89.27	740.64	111.75	3238	4.38	5.15
KD 4-19	69.91	405.76	39.95	214.45	129.21	50.65	255.21	59.13	464.84	131.99	518.08	107.59	1011.11	176.15	3634	7.68	2.86
KD 4-21	19.99	91.19	9.40	48.07	31.05	9.28	73.08	17.43	167.86	51.18	204.37	42.39	391.67	68.61	1226	6.65	2.41

Table 2 (*continued*)

Spots no.	Element (ppm)														ΣREE	Ratio	
	La	Ce	Pr	Nd	Sm	Eu	Gd	Tb	Dy	Ho	Er	Tm	Yb	Lu		Ce/Ce*	(Sm/La)N
KD 4-22	8.18	81.30	8.49	50.04	40.60	13.20	98.15	24.72	211.48	58.94	221.87	46.27	415.51	72.99	1352	9.76	7.69
KD 4-23	14.28	142.21	14.31	85.28	60.49	21.37	152.86	37.29	319.30	88.37	321.95	66.30	581.77	96.23	2002	9.95	6.56
KD 4-25	15.12	108.05	11.71	71.73	56.67	19.11	133.46	32.53	295.20	92.69	356.80	77.57	715.22	118.24	2104	8.12	5.81
KD 4-26	163.83	367.30	45.14	202.00	70.42	22.47	139.24	30.60	274.02	85.00	337.86	71.20	665.73	112.78	2588	4.27	0.67
KD 4-28	9.96	123.77	12.52	79.71	73.73	25.21	177.79	43.86	362.16	95.30	334.32	67.58	580.80	93.58	2080	11.09	11.47
KD 4-29	17.20	148.75	14.65	84.15	56.52	17.32	144.26	36.18	299.53	75.99	270.75	53.20	446.59	72.06	1737	9.37	5.09
KD 4-04	0.46	2.87	0.60	4.47	5.44	0.49	41.39	12.82	133.30	47.00	198.04	40.08	332.18	58.01	877	5.45	18.13
KD 4-13	0.25	2.76	0.91	8.19	14.07	4.80	39.92	12.82	99.06	24.17	70.38	12.45	90.90	14.09	395	5.79	86.80

Most of the zircon crystals in sample KD 4 show moderate positive Ce anomaly, negative Eu anomaly and LREE depletion. Their total REE contents range from 395 to 3634 ppm. Zircon grains from this sample dominantly show high La contents (5.81–163.83 ppm), low $(Sm/La)_N$ (0.67–11.47) and Ce/Ce* (4.27–11.13) values, similar to hydrothermal zircon. The LREE enrichment in zircon grains from this sample is also correlated with higher age discordance. Two Paleoproterozoic grains (1826 Ma and 1767 Ma) show low La contents (0.46 and 0.25 ppm), high $(Sm/La)_N$ (18.13 and 86.80) and Ce/Ce*(5.45 and 5.79), with low LREE.

5. Discussion

The rock types in our study area display several diagnostic features of an impact event. Brecciation and melting are quite obvious and the resultant brecciated granite, melt breccia, and dacite to rhyolite rocks formed from the host granite occur widely, occupying the crater floor. However, the presence of deformational textures like ballen quartz, checkerboard feldspar, kinked feldspar, glassy flow banding, PF are mainly seen in the topmost units such as the dacite to rhyolite, and melt breccia, supporting the general view of high effect of impact on the upper surface. Some of the deformational features and textures observed in our study were earlier reported by Pati et al. (2008). Based on the previous observations and those in our present study, it is obvious that the impact severity decreases downwards from dacite-rhyolite to melt breccia to brecciated granite and finally to basement granite. PFs, usually formed at high temperature-pressure conditions, are mainly seen in dacite to rhyolite and melt breccia whereas checkerboard feldspar, characteristic of less impact pressure, are obvious in brecciated granite and the basement granite are devoid of impact related deformation features.

5.1. Geochemical evidence for impactite origin

The various rock types in Dhala, apart from their K_2O variation, exhibit similar major and trace element characteristics, suggesting their genetic link and also relation with the impact event. The 'abnormal' enrichment of K_2O and contrary depletion of Na_2O and CaO in dacite to rhyolite melt rocks, and melt breccia, might suggest element redistribution induced by meteorite impact. Intense and pervasive potassic metasomatism associated with terrestrial impact structures were well-documented from various parts of the world and have been summarized in Naumov (2002). Several other recent reports of impact-related potassium metasomatism are reported from Ilyinets, Ukraine (Gurov et al., 1998), Ries crater, Germany (Osinski, 2005), Siljan, Sweden (Reimold et al., 2005) and from Rochechouart, France (Schmieder et al., 2010). Studies on impact-related hydrothermal alteration have shown that primary plagioclase in granitic rocks is generally replaced by orthoclase aggregates. K-feldspar formation in impactites is understood to be due to release of potassium during post-impact hydrothermal alteration processes involving the melt rocks (e.g., Grieve, 1994; McCarville and Crossey, 1996; Gurov et al., 1998; Masaitis et al., 1999; Naumov, 2002; Vishnevsky and Montanari, 1999).

The high alkali contents are likely due to the susceptibility of glass to fluid-rock interaction, which promoted more intense post-impact hydrothermal alteration and associated mass transfer. In particular, there is a more extreme Na_2O depletion and less severe enrichment of K_2O, presumably reflecting variable Na_2O-K_2O mass exchange during hydrothermal alteration. All rocks in the vicinity of the crater have undergone variable degrees of K-metasomatism. The brecciated granite shows only a moderate increase in K_2O; however, the melt breccias and dacite to rhyolite rocks show moderate to high enrichment in K_2O, which is inferred to be the result of impact-related and post-impact hydrothermal alteration. This process of K-metasomatism can be exemplified through the igneous spectrum plots (after Hughes, 1973) (Fig. 16). The granitoids are relatively less altered as compared to the volcanics. Melt breccia and dacite to rhyolite rocks show extreme potassic alteration.

The reddish colour of the impactites in the Dhala area is clear field evidence for pervasive K-metasomatism. It is inferred that the original target rocks (i.e. granite), which have a high content of potassium minerals like biotite were transformed to K-feldspar at high temperatures; apart from the already present K-feldspar. Subsequently, during prolonged cooling-related hydrothermal alteration, secondary K-feldspars like adularia could form and occupy intergranular spaces and fractures. The formation of secondary K-feldspar in the impactites and associated rocks resulted in high whole-rock K_2O content.

The observed depletion in Na_2O in the Dhala impactites is possibly related to alteration of plagioclase to sericite during hydrothermal activity. Similarly, Ca-rich minerals like hornblende are susceptible to alteration to chlorite, which may account for the depletion of CaO in the rocks. Sodium and calcium depletion by such processes have been previously described in impactites elsewhere.

5.2. Zircon morphology, geochronology and trace element evidence of impactites

It is the first time that zircon grains from Dhala were carefully analyzed in terms of their morphology and structure. Reidite, a high pressure polymorph of zircon, is also identified in brecciated granite. The rarity of this mineral that is distinctly diagnostic of an impact event provides, perhaps, the most robust evidence that these rocks were formed by shock metamorphism through impact. The PFs in this reidite might have formed under high temperature-pressure regime by a process such as meteorite impact. The Raman spectra correspond to a combination of zircon and reidite, with characteristic minor peaks of reidite and typical zircon peaks at 974 and 1008 cm^{-1}. The persistence of peaks at 974 and 1008 cm^{-1} are from the remaining untransformed zircons (Van Westrenen et al., 2004; Gucsik et al., 2004b). This *co*-existence of polymorphs has been tested in the laboratory in previous studies, and the shock pressure required for such co-existence is reported by Gucsik et al. (2004a) as 38 GPa. It is revealed that zircon also exhibits typical deformational features like PDFs, cracks, melting and quenching, and Pb loss.

Regarding the isotopic age data, zircon grains from dacite to rhyolite (KD 48) show an upper intercept age at 2499 ± 27 Ma and weighted mean $^{207}Pb/^{206}Pb$ age of 2482 ± 40 Ma. Zircons from melt breccia sample (KD 51) yield upper intercept age of 2493 ± 36 Ma. Zircons from the

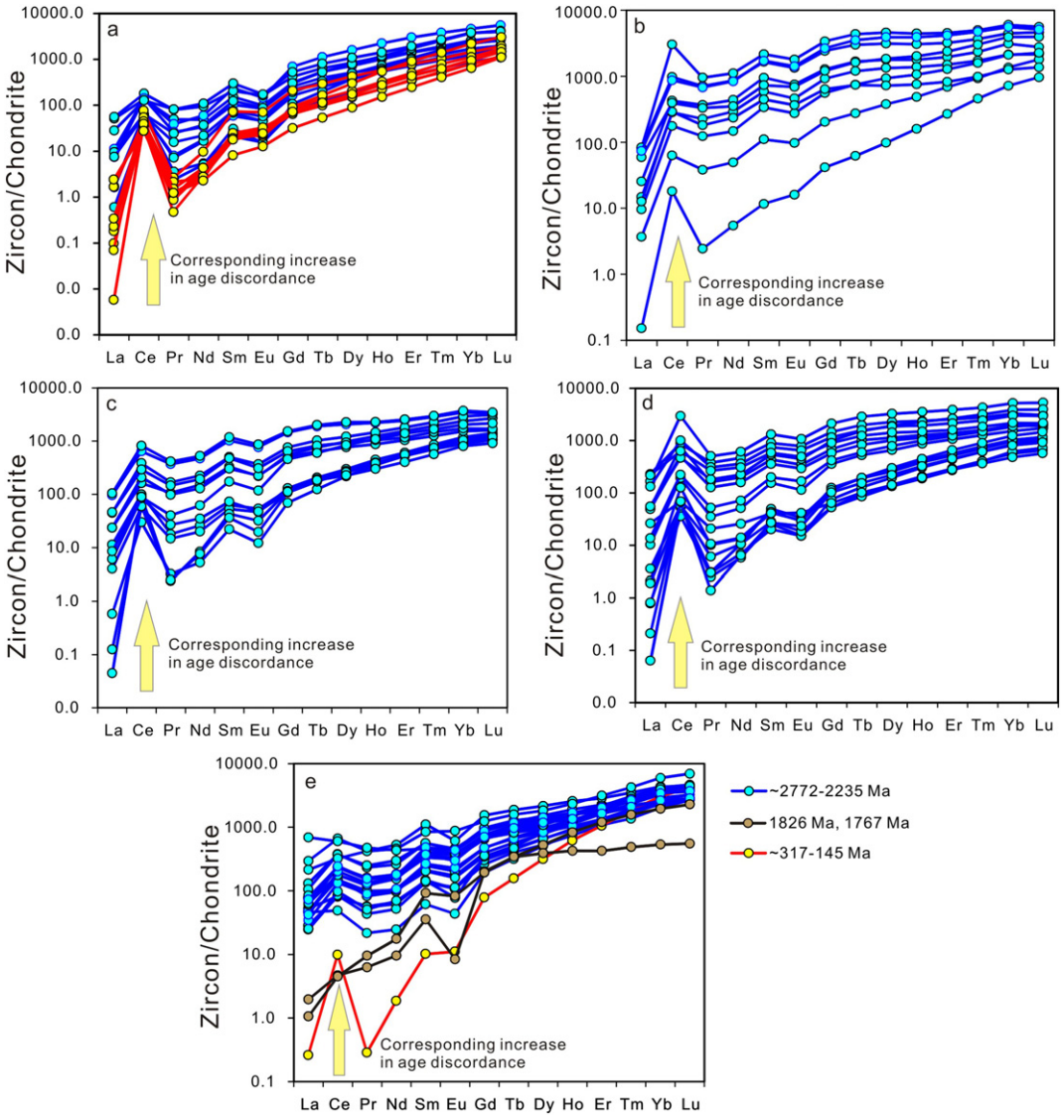


Fig. 15. Chondrite-normalized REE diagrams showing the REE content of detrital cores and metamorphic rims. (a) KD 73, (b) KD 51, (c) KD 57, (d) KD 48, (e) KD 4. Chondrite values are after Sun and McDonough (1989). The arrow indicates that with the increase in LREE content, there is a corresponding age discordance in the zircon U-Pb data of Archean grains.

other melt breccia sample (KD 57) show upper intercept $^{207}Pb/^{206}Pb$ age of 2470 ± 26 Ma with weighted mean $^{207}Pb/^{206}Pb$ age of 2463 ± 36 Ma. Zircons from brecciated granite (KD 73) show three groups at 2648 ± 57 Ma, 2467 ± 21 Ma and 150 ± 11 Ma. Zircons from the quartz reef sample (KD4), occurring along the outer rim of the crater, can be divided into three groups. One group has $^{207}Pb/^{206}Pb$ age range from 2772 to 2550 Ma with seven spots defining an upper intercept age at 2679 ± 140 Ma (MSWD = 0.89, n = 7). Another group yields $^{207}Pb/^{206}Pb$ age range of 2483–2235 Ma, with six spots yielding an upper intercept age at 2443 ± 93 Ma (MSWD = 0.42, n = 6). Two spots show $^{207}Pb/^{206}Pb$ ages of 1826 ± ~~48~~ 97 Ma and 1767 ± 100 Ma and one spot shows $^{206}Pb/^{238}U$ age of 317 ± 10 Ma.

Since the lower intercept is not defined in the concordia plot, the age of the impact event can only be assumed. The zircons obtained from the xenocrysts of basement granite show an age of 2648 ± 57 Ma. Similar age of basement granite is also reflected in the zircons separated from the quartz reef (2679 ± 140 Ma). Zircon U-Pb age of the granite sample at 2467 ± 21 Ma, those from two melt breccias at 2493 ± 36 Ma and 2470 ± 26 Ma, and dacite to rhyolite at 2499 ± 27 Ma, indicate magma emplacement of this igneous complex at around 2.5 Ga. Pati et al. (2010) reported SHRIMP U-Pb zircon ages of 2.56 Ga and 2.55 Ga for the emplacement age of the granite. Mondal et al. (2002) reported 2.49 Ga from the leucogranitoid which is close to the upper intercept age of 2.46 Ga from zircons in the brecciated granite of our study. The emplacement of the granite is, therefore, broadly consistent with an age of ca. 2.5 Ga, with subsequent Pb loss. Field evidence suggests that the quartz reefs are brecciated at several places providing clues on

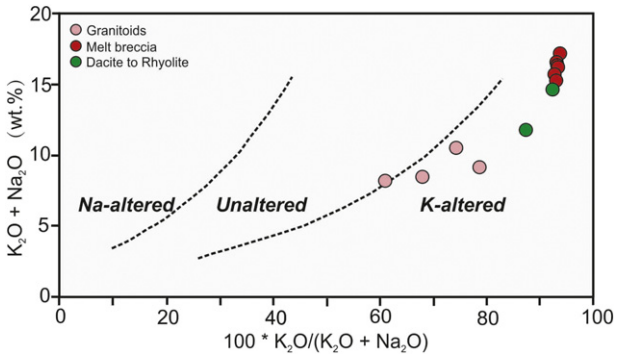


Fig. 16. Igneous spectrum diagram for all the lithounits of the study area. (After Hughes, 1973)

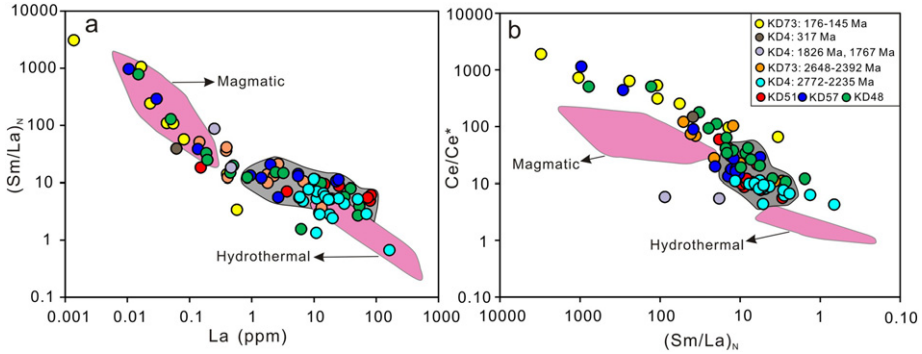


Fig. 17. Discrimination plots for magmatic and hydrothermal zircon grains. (a) La~$(Sm/La)_N$ and Ce/Ce*, (b) $(Sm/La)_N$ ~Ce/Ce*. Pink field are from Hoskin (2005) and the gray fields are from present study. The data indicate transition from magmatic to hydrothermal zircons.

impact related phenomena in this rock. The NE-SW trending quartz reefs and NW-SE trending mafic dikes persist throughout the Bundelkhand craton at regular intervals (Bhattacharya and Singh, 2013). They are younger than the Bundelkhand granites and have been considered as Proterozoic intrusions (Pati et al., 2007; Rao et al., 2005). The presence of clasts of quartz reef and mafic dikes from the Dhala impact structure clearly suggest that the impact is subsequent to mafic dike emplacement. Pati et al. (2008, 2010) suggested that that the impact occurred between 2.55 Ga and 1.7 Ga. However zircon grains from the quartz reef of our samples located in the boundary of the impact crater are inferred to preserve all the chronological events as most of the reefs occupy the outer rim of the crater and the age data from these rocks are clustered into three groups. The old group of 2772–2550 Ma correspond to the basement magmatism. The major group cluster yields $^{207}Pb/^{206}Pb$ age range from 2483 to 2235 Ma, and define an upper intercept age at 2443 ± 93 Ma, and the youngest age in this group is 2235 Ma. The impact time is also identified in our dacite to rhyolite sample which yield $^{207}Pb/^{206}Pb$ age of 2383 Ma and 2366 Ma indicating new zircon growth. The impact time thus be constrained to be between ca.2.44 Ga and ca.2.24 Ga. The two concordant spots in quartz reef showing $^{207}Pb/^{206}Pb$ ages of 1826 ± 97 Ma and 1767 ± 100 Ma from unfractured grains indicate a post-impact thermal event (Figs. 15 and 17) (Sarangi et al., 2004). Although a minor younger population of Phanerozoic zircon grains are also noted in some of the rocks that we analyzed, the fact that the Proterozoic sediments deposited on the crater basement are unaffected by the impact suggests that these younger ages do not correspond to the impact event.

Zircon grains in our samples are characterized by high and variable REE contents, with a positive Ce anomaly, and negative Eu anomaly. The Neoarchean to early Paleoproterozoic zircon grains show high LREE contents, particularly marked enrichment in La, together with low $(Sm/La)_N$ and Ce/Ce* values compatible with the features of hydrothermal zircon (Hoskin, 2005). The Neoarchean to early Paleoproterozoic zircon grains from samples KD 51, KD 57, KD 48 and KD 4 dominantly fall within the field of hydrothermal zircon in the $(Sm/La)_N$ vs. La plots (Fig. 17a). However, most of the samples fall in the transitional area between magmatic and hydrothermal zircon in the Ce/Ce* vs. $(Sm/La)_N$ (Fig. 17b). The younger group of Phanerozoic zircon grains from KD 73 and KD 4 fall along the magmatic field, indicating a closed system during zircon overgrowth (Hoskin, 2005; Martin et al., 2008). The correlation among increasing LREE contents, degree of age discordance, and intensity of micro-fractures within the grains suggest an open system for the mobility of REE, leading to the incorporation of more LREE during zircon dissolution and reprecipitation (Martin et al., 2008). The high K_2O content of the samples also suggests that the peralkaline environment promoted recrystallization of the Neoarchean to early Paleoproterozoic hydrothermal zircon grains (Rubin et al., 1989). The fluids that caused the recrystallization might have been sourced from the impact event.

6. Conclusions

This study provides further insights into the meteorite impact origin for the Dhala structure. An integrated investigation based on petrological, geochemical and zircon geochronological data lead to the following major conclusions:

The impactites of Dhala structure, based on clast-matrix ratio, can be classified into three varieties namely, (a) clast-rich unit represented by the brecciated granite (b) nearly equal clast-matrix proportion represented by the melt breccia, and (c) clast poor and matrix-rich variety represented by the dacite to rhyolite rock.

Geochemistry of impactites suggests pervasive K_2O metasomatism, which we correlate with the impact event at high temperatures.

Reidite, a high pressure polymorph of zircon, was identified in our sample. Reidite occurs together with untransformed zircon.

Zircon U-Pb data indicate magmatic emplacement of the basement rocks at around 2.50–2.47 Ga. The impact time is constraint to be between ca. 2.44 Ga and ca. 2.24 Ga. A minor younger group of concordant grains with ages of 1826 ± 97 Ma and 1767 ± 100 Ma represent unfractured grains formed during a thermal event after the impact event. The REE patterns of zircon grains are also suggestive of a hydrothermal recrystallization in the presence of alkali-enriched fluids, with high La content and low $(Sm/La)_N$ and Ce/Ce* values.

Supplementary data to this article can be found online at https://doi.org/10.1016/j.gr.2017.10.006.

Acknowledgements

We thank Associate Editor Prof. Sanghoon Kwon and three anonymous referees for their constructive comments that improved our manuscript. Keerthy acknowledges Kerala State Council for Science Technology and Environment, Government of Kerala, India, for providing research grant (Order No. 476/2016/KSCSTE) for this study. Thanks to Akhil, Ambadi, Akhila, and students of MSc Geology (2015–17 batch) of University of Kerala for accompanying to the field. Santosh is supported by Foreign Expert funding from China University of Geosciences Beijing, China and Professorial position at the University of Adelaide, Australia. Sajinkumar thank University Grants Commission (UGC), Government of India, for granting Raman Post-Doctoral Fellowship (No 5-56/2016(IC)) which enabled him to carry out the Post-Doctoral

Research work at Michigan Technological University, USA. Facility of LERIS, University of Kerala, India has also been utilized for this work.

References

Alvarez, L.W., Alvarez, W., Asaro, F., Michel, H.V., 1980. Extraterrestrial cause for the Cretaceous-Tertiary extinction. Science 208, 1095–1108.

Basu, A.K., 1986. Geology of Bundelkhand granite massif, Central India. Geological Survey of India Records 101, 61–124.

Bermúdez, H.D., García, J., Stinnesbeck, W., Keller, G., Rodríguez, J.V., Hanel, M., Hopp, J., Schwarz, W.H., Trieloff, M., Bolívar, L., Vega, F.J., 2016. The Cretaceous-Palaeogene boundary at Gorgonilla Island, Columbia, South America. Lithos 28, 83–90.

Bhattacharya, A.R., Singh, S.P., 2013. Proterozoic crustal scale shearing in the Bundelkhand massif with special reference to quartz reefs. Journal of the Geological Society of India 82, 474–484.

Bhattacharya, D., Parihar, P.S., Sinha, R.M., Sen, D.B, 2006. Geochemical approach for exploration in Mohar Collapsed Cauldron, Shivpuri district, Madhya Pradesh, India: A study for potential Fe-oxide breccia hosted U-Cu mineralization. IAEA Symposium, Jaduguda.

Bischoff, A., Stöffler, D., 1984. Chemical and structural changes induced by thermal annealing of shocked feldspar inclusions in impact melt rock from Lappajärvi crater, Finland. Journal of Geophysical Research 89, B645–B656.

Blenkinsop, T.G., 2000. Deformation Microstructures and Mechanisms in Minerals and Rocks. Elsevier, New York, p. 164.

Blum, J.D., 1993. Zircon can take the heat. Nature 366, 718.

Bowring, S.A., Erwin, D.H., Jin, Y.G., Martin, M.W., Davidek, Wang, W., 1998. U/Pb zircon geochronology and tempo of the end-Permian mass extinction. Science 280, 1039–1045.

Bracciali, L., Parrish, R., Horstwood, M.S.A., Condon, D.J., Najman, Y., 2013. U-Pb LA-(MC)-ICP-MS dating of rutile: new reference materials and applications to sedimentary provenance. Chemical Geology 347, 82–101.

Corfu, F., Hanchar, J.M., Hoskin, P.W., Kinny, P., 2003. Atlas of zircon textures. Reviews in Mineralogy and Geochemistry 53, 468–500.

Dawson, P., Hargreave, M.M., Wilkinson, G.F., 1971. The vibrational spectrum of zircon ($ZrSiO_4$). Journal of Physics C: Solid State Physics 4, 240–256.

Ferrière, L., Koeberl, C., Reimold, W.U., 2009. Characterisation of ballen quartz and cristobalite in impact breccias: new observations and constraints on ballen formation. European Journal of Mineralogy 21, 203–217.

French, B.M., Koeberl, C., 2010. The convincing identification of terrestrial meteorite impact structures: what works, what doesn't, and why. Earth-Science Reviews 92, 123–170.

Gibson, R.L., Armstrong, R.A., Reimold, U.W., 1997. The age and thermal evolution of the Vredefort impact structure: a single-grain U–Pb zircon study. Geochimica et Cosmochimica Acta 61, 531–1540.

Glass, B.P., 2002. Upper Eocene impact ejecta/spherule layers in marine sediments. Chemie der Erde 62, 173–196.

Govindaraju, K., 1994. 1994 compilation of working values and sample description for 383 geostandards. Geostandards and Geoanalytical Research 18 (S1), 1–158.

Grieve, R.A.F., 1975. Petrology and chemistry of the impact melt at Mistastin Lake crater, Labrador. GSA Bulletin 86, 1617–1629.

Grieve, R.A.F., 1994. An impact model of the Sudbury structure. In: Lightfoot, P.C., Naldrett, A.J. (Eds.), Proceedings of the Sudbury-Noril'sk Symposium. Special Vol. 5. Ontario Geological Survey, Toronto, pp. 119–132.

Gucsik, A., Koeberl, C., Brandstätter, F., Libowitzky, E., Zhang, M., 2004a. Infrared, Raman, and cathodoluminescence studies of impact glasses. Meteoritics and Planetary Sciences 39, 1273–1285.

Gucsik, A., Zhang, M., Koeberl, C., Salje, E.K.H., Redfern, S.A.T., Pruneda, J.M., 2004b. Infrared and raman spectra of $ZrSiO_4$ experimentally shocked at high pressures. Mineralogical Magazine 68 (5), 801–811.

Gurov, E.P., Koeberl, C., Reimold, W.U., 1998. Petrography and geochemistry of target rocks and impactites from the Ilyinets crater, Ukraine. Meteoritics and Planetary Science 33, 1317–1333.

Hamers, M.F., Pennock, G.M., Herwegh, M., Drury, M.R., 2016. Distinction between amorphous and healed planar deformation features in shocked quartz using composite color scanning electron microscope cathodoluminescence (SEM-CL) imaging. Meteoritics and Planetary Science 51 (10), 1914–1931.

Hirth, G., Tullis, J., 1994. The brittle-plastic transition in experimentally deformed quartz aggregates. Journal of Geophysical Research 99, 11,731–11,747.

Horstwood, M.S.A., Košler, J., Gehrels, G., Jackson, S.E., Mclean, N.M., Paton, C., Pearson, N.J., Sircombe, K., Sylvester, P., Vermeesch, P., Bowring, J.F., Condon, D.J., Schoene, B., 2016. Community-derived standards for LA-ICP-MS U-(Th-)Pb geochronology - uncertainty propagation, age interpretation and data reporting. Geostandards and Geoanalytical Research 40, 311–332.

Hoskin, P.W.O., 2005. Trace-element composition of hydrothermal zircon and the alteration of Hadean zircon from the Jack Hills, Australia. Geochimica et Cosmochimica Acta 69 (3), 637–648.

Hu, Z.C., Liu, Y.S., Gao, S., Xiao, S.Q., Zhao, L.S., Günther, D., Li, M., Zhang, W., Zong, K.Q., 2012. A "wire" signal smoothing device for laser ablation inductively coupled plasma mass spectrometry analysis. Spectrochimica Acta Part B: Atomic Spectroscopy 78 (0), 50–57.

Huffman, A.R., Reimold, W.U., 1996. Experimental constraints on shock-induced microstructures in naturally deformed silicates. Tectonophysics 236, 165–217.

Hughes, C.J., 1973. Spilites, keratophyres and the igneous spectrum. Geological Magazine 109, 513–527.

Jain, S.C., Gaur, V.P., Srivastava, S.K., Nambiar, K.V., Saxena, H.P., 2001. Recent find of a cauldron structure in Bundelkhand craton. Geological Survey of India Special Publication 64, 289–297.

Kalleson, E., Corfu, F., Dypvik, H., 2009. U–Pb systematics of zircon and titanite from the Gardnos impact structure, Norway: evidence for impact at 546 Ma? Geochimica et Cosmochimica Acta 73, 3077–3092.

Kamo, S.L., Reimold, W.U., Krogh, T.E., Colliston, W.P., 1996. A 2.023 Ga age for the Vredefort impact event and a first report of shock metamorphosed zircons in pseudotachylitic breccias and granophyre. Earth and Planetary Science Letters 144, 369–387.

Knittle, E., Williams, Q., 1993. High-pressure Raman-spectroscopy of $ZrSiO_4$—observation of the zircon to scheelite transition at 300 K. American Mineralogist 78, 245–252.

Koeberl, C., 2007. The geochemistry and cosmochemistry of impacts. In: Davis, A. (Ed.), Treatise of Geochemistry. Vol. 1. Elsevier, New York, NY:pp. 1.28.1–1.28.52. https://doi.org/10.1016/B978-008043751-4/00228-5 (online edition).

Koeberl, C., Reimold, W.U., Shirey, S.B., 1998. The Aouelloul crater, Mauritania: on the problem of confirming the impact origin of a small crater. Meteoritics and Planetary Science 33, 513–517.

Koeberl, C., Claeys, P., Hecht, L., McDonald, I., 2012. Geochemistry of impactites. Elements 8 (1), 37–42.

Krishna, A.K., Murthy, N.N., Govil, P.K., 2007. Multi-element analysis of soils by wavelength-dispersive X-ray fluorescence spectrometry. Atomic Spectroscopy 28, 202–214.

Krogh, T.E., Davis, D.W., Corfu, F., 1984. Precise U–Pb zircon and baddeleyite ages for the Sudbury area. In: Pye, E.G., Naldrett, A.J., Giblin, P.E. (Eds.), The Geology and Ore Deposits of the Sudbury Structure. Ontario Geol. Survey Spec. vol. 1, pp. 431–447.

Krogh, T.E., Kamo, S.L., Sharpton, V.L., Marin, L.E., Hildebrand, A.R., 1993a. U-Pb ages of single shocked zircons linking distal K/T ejecta to the Chicxulub crater. Nature 366, 731–734.

Krogh, T.E., Kamo, S.L., Bohor, B.F., 1993b. Fingerprinting the K/T impact site and determining the time of impact by U–Pb dating of single shocked zircons from distal ejecta. Earth and Planetary Science Letters 119, 425–429.

Kumar, S., Yi, K., Raju, K., Pathak, M., Kim, N., Lee, T.H., 2011. SHRIMP U–Pb geochronology of felsic magmatic lithounits in the central part of Bundelkhand Craton, Central India. In: Molina, J.F.S., Scarrow, J.H., Bea, F., Montero, P. (Eds.), 7th Hutton Symposium on Granites and Related Rocks Avila, Spain, p. 83.

Leroux, H., Reimold, W.U., Doukhan, J.-C., 1994. A TEM investigation of shock metamorphism of quartz from the Vredefort Dome, South Africa. Tectonophysics 230, 223–239.

Liu, Y.S., Hu, Z.C., Gao, S., Günther, D., Xu, J., Gao, C.G., Chen, H.H., 2008. In situ analysis of major and trace elements of anhydrous minerals by LA-ICP-MS without applying an internal standard. Chemical Geology 257 (1–2), 34–43.

Liu, Y.S., Gao, S., Hu, Z.C., Gao, C.G., Zong, K.Q., Wang, D.B., 2010. Continental and oceanic crust recycling-induced melt-peridotite interactions in the Trans-North China Orogen: U-Pb dating, Hf isotopes and trace elements in zircons of mantle xenoliths. Journal of Petrology 51 (1&2), 537–571.

Long, X.P., Sun, M., Yuan, C., Kröner, A., Hu, A.Q., 2012. Zircon REE patterns and geochemical characteristics of Paleoproterozoic anatectic granite in the northern Tarim Craton, NW China: implications for the reconstruction of the Columbia supercontinent. Precambrian Research 222–223, 474–487.

Ludwig, K.R., 2003. ISOPLOT 3.00: A Geochronological Toolkit for Microsoft Excel. Berkeley Geochronology Center, California, Berkeley (39 pp).

Manikyamba, C., Ray, J., Ganguly, S., Singh, M.R., Santosh, M., Saha, A., Satyanarayanan, M., 2015. Boninitic metavolcanic rocks and island arc tholeiites from the Older Metamorphic Group (OMG) of Singhbhum Craton, eastern India: geochemical evidence for Archean subduction processes. Precambrian Research 271, 138–159.

Martin, L.A.J., Duchene, S., Deloule, E., Vanderhaeghe, O., 2008. Mobility of trace elements and oxygen in zircon during metamorphism: consequences for geochemical tracing. Earth and Planetary Science Letters 267, 161–174.

Maruyama, S., Ebisuzaki, T., 2016. Origin of the Earth: a proposal of new model called ABEL. Geoscience Frontiers https://doi.org/10.1016/j.gsf.2016.10.005.

Maruyama, S., Santosh, M., 2017. Frontiers in early Earth history and primordial life – part I. Geoscience Frontiers https://doi.org/10.1016/j.gsf.2016.12.002.

Maruyama, S., Santosh, M., Azuma, S., 2016. Initiation of plate tectonics in the Hadean: eclogitization triggered by the ABEL Bombardment. Geoscience Frontiers https://doi.org/10.1016/j.gsf.2016.11.009.

Masaitis, V.L., Naumov, M.V., Mashchak, M.S., 1999. Anatomy of the Popigai impact crater, Russia. In: Dessler, B.O., Sharpton, V.L. (Eds.), Large Meteorite Impacts and Planetary Evolution II, Special Paper 339. Geological Society of America, Boulder, pp. 1–17.

McCarville, P., Crossey, L.J., 1996. Post-impact hydrothermal alteration of the Manson impact structure. In: Koeberl, C., Anderson, R.R. (Eds.), The Manson Impact Structure: Anatomy of an Impact Crater. Special Paper 302. Geological Society of America, Boulder, pp. 347–376.

Melosh, H.J., 1989. Impact Cratering: A Geologic Process. Oxford University Press, New York, NY (245 pp).

Mittlefehldt, D.W., Hörz, F., See, T.H., Scott, E.R.D., Mertzman, S.A., 2005. Geochemistry of target rocks, impact-melt particles, and metallic spherules from Meteor Crater, Arizona: empirical evidence on the impact process. In: Kenkmann, T., Hörz, F., Deutsch, A. (Eds.), Large Meteorite Impacts III. Special Paper, vol. 384. Geological Society of America, Boulder, CO, pp. 367–390.

Mohan, M.R., Singh, S.P., Santosh, M., Siddiqui, M.A., Balaram, V., 2012. TTG suite from the Bundelkhand craton, central India: geochemistry, petrogenesis and implications for Archean crustal evolution. Journal of Asian Earth Sciences 58, 38–50.

Mondal, M.E.A., Goswami, J.N., Deomurari, Sharma, K.K., 2002. Ion microprobe $^{207}Pb/^{206}Pb$ ages of zircons from the Bundelkhand massif, northern India: implications for crustal evolution of the Bundelkhand-Aravalli protocontinent. Precambrian Research 117, 85–100.

Naumov, M.V., 2002. Impact-generated hydrothermal systems: data from Popigai, Kara, and Puchezh-Katunki impact structures. In: Plado, J., Pesonen, L.J. (Eds.), Impacts in Precambrian Shields. Springer Verlag, Heidelberg, pp. 117–172.

Osae, S., Misra, S., Koeberl, C., Sengupta, D., Ghosh, S., 2005. Target rocks, impact glasses, and melt rocks from the Lonar impact crater, India: petrography and geochemistry. Meteoritics and Planetary Science 40, 1473–1492.
Osinski, G.R., 2005. Hydrothermal activity associated with the Ries impact event, Germany. Geofluids 5, 202–220.
Osinski, G.R., Spray, J.G., 2001. Impact-generated carbonate melts: evidence from the Haughton impact structure, Arctic Canada. Earth and Planetary Science Letters 194, 17–29.
Pati, J.K., 2005. The Dhala structure, Bundelkhand craton, Central India—a new large Paleoproterozoic impact structure (abstract). Meteoritics and Planetary Science 40, A121.
Pati, J.K., Raju, S., Pruseth, K.L., Malviya, V.P., Arima, M., Pati, P., Prakash, K., 2007. Geology and geochemistry of giant quartz veins from the Bundelkahand craton, Central India and its implications. Journal of Earth System Science 116, 497–510.
Pati, J.K., Reimold, W.U., Koeberl, C., Pati, P., 2008. The Dhala structure, Bundelkhand craton, Central India-eroded remnant of a large Paleoproterozoic impact structure. Meteoritics and Planetary Science 43 (8), 1383–1398.
Pati, J.K., Jourdan, F., Armstrong, R.A., Reimold, W.U., Prakash, K., Renne, P.R., 2010. First SHRIMP U-Pb and $^{40}Ar/^{39}Ar$ chronological results from impact melt breccia from the Paleoproterozoic Dhala impact structure, India. Special Paper of the Geological Society of America 465, 571–591.
Pati, K.K., Reimold, W.U., Greshake, A., Schmitt, R.T., Koeberl, C., Pati, P., Prakash, K., 2016. Pseudotachylitic breccia from the Dhala impact structure, north-central India: texture, mineralogy and geochemical characterization. Tectonophysics 649, 18–32.
Rao, M.J., Rao, P.G.V.S., Widdowson, M., Kelley, S.P., 2005. Evolution of Proterozoic mafic dyke swarms of Bundelkhand craton, Central India. Current Science 88, 502–506.
Ray, L., Nagaraju, P., Singh, S.P., Ravi, G., Roy, S., 2016. Radioelemental, petrological and geochemical characterization of the Bundelkhand craton, central India: implication in the Archean geodynamic evolution. International Journal of Earth Sciences 105, 1087–1107.
Reimold, W.U., 1982. The Lappajärvi meteorite crater, Finland; petrography, Rb-Sr, major and trace element geochemistry of the impact melt and basement rocks. Geochimica et Cosmochimica Acta 46 (7), 1203–1225.
Reimold, W.U., Leroux, H., Gibson, R.L., 2002. Shocked and thermally metamorphosed zircon from the Vredefort impact structure, South Africa. European Journal of Mineralogy 14, 859–868.
Reimold, W.U., Kelley, S.P., Sherlock, S.C., Henkel, H., Koeberl, C., 2005. Laser argon dating of melt breccias from the Siljan impact structure, Sweden: implications for a possible relationship to Late Devonian extinction events. Meteoritics and Planetary Science 40, 591–607.
Roy, M., Kumar, S., Pandey, P., Bhairam, C.L., Parihar, P.S., 2014. Petrological evidences of impact-induced shock metamorphism in the basement granitoids and rhyolitic melt breccia of Mohar area, Shivpuri district, Madhya Pradesh. Journal Geological Society of India 84, 377–384.
Rubin, J.N., Henri, C.D., Price, J.G., 1989. Hydrothermal zircons and zircon overgrowths, Sierra Blanca Peaks, Texas. American Mineralogist 74, 865–869.
Saha, L., Freis, D., Gerdes, A., Pati, J.K., Sarkar, S., Patole, V., Bhandari, A., Nasipuri, P., 2016. Crustal geodynamics from the Archean Bundelkhand Craton, India: constraints from zircon U-Pb-Hf isotope studies. Geological Magazine 153 (1), 179–192.
Santosh, M., Arai, T., Maruyama, S., 2017. Hadean Earth and primordial continents: the cradle of prebiotic life. Geoscience Frontiers 8:309–327. https://doi.org/10.1016/j.gsf.2016.07.005.
Sarangi, S., Gopalan, K., Kumar, S., 2004. Pb-Pb age of earliest megascopic eukaryotic alga–bearing Rohtas Formation, Vindhyan Supergroup, India: implications for Precambrian atmospheric oxygen evolution. Precambrian Research 132, 107–121.
Schmieder, M., Buchner, E., Schwarz, W.H., Trieloff, M., Lambert, P., 2010. A Rhaetian 40Ar/39Ar age for the Rochechouart impact structure (France) and implications for the latest Triassic sedimentary record. Meteoritics and Planetary Science 45 (8), 1225–1242.
Sharma, K.K., Rahman, A., 2000. The early Archaean-Paleoproterozoic crustal growth of the Bundelkhand craton, northern Indian shield. In: Deb, M. (Ed.), Crustal Evolution and Metallogeny in the Northwestern Indian Shield. Narosa Publishing House, New Delhi, pp. 51–72.
Silva, D., Lana, C., de Souzo Filho, C.R., 2016. Petrographic and geochemical characterization of the granitic rocks of the Araguainha impact crater, Brazil. Meteoritics and Planetary Science 51 (3), 443–467.
Singh, S.P., Bhattacharya, A.R., 2017. N-S crustal shear system in the Bundelkhand massif: a unique crustal evolution signature in the northern Indian. Peninsula Journal Earth Syst. Sciences (accepted).
Singh, S.P., Dwivedi, S.B., 2015. High grade metamorphism in the Bundelkhand massif and its implications on Mesoarchean crustal evolution in Central India. Journal of Earth System Science 124, 197–211.
Singh, S.P., Singh, M.M., Srivastava, G.S., Basu, A.K., 2007. Crustal evolution in Bundelkhand area, Central India. Journal of Himalayan Geology 28, 79–101.
Singh, S.P., Bhattacharya, A.R., Hemraj, Shrivastava, S.K., 2010. Structural development of a granite collapse breccia of Mohar, Bundelkhand massif: an evidence of a Precambrian caldera from the Indian Shield. Journal of Economic Geology and Georesource Management 7 (1–2), 105–117.
Spencer, C.J., Kirkland, C.L., Taylor, R.J., 2016. Strategies towards statistically robust interpretations of in situ U–Pb zircon geochronology. Geoscience Frontiers 7, 581–589.
Srivastava, S.K., Nambiar, K.V., 2003. 3D characterization of the Mohar cauldron, Shivpuri District, Madhya Pradesh. Geological Survey of India Records 136, 52–54.
Sun, S.S., McDonough, W.F., 1989. Chemical and isotopic systematics of oceanic basalts: implications for mantle composition and processes. In: Saunders, A.D., Norry, M.J. (Eds.), Magmatism in Ocean Basins. Special Publication. vol. 42. Geological Society of London, pp. 313–345.
Timms, N.E., Erickson, T.M., Pearce, M.A., Cavosie, A.J., Schmieder, M., Tohver, E., Reddy, S.M., Zanetti, M.R., Nemchin, A.A., Wittman, A., 2017. A pressure-temperature phase diagram for zircon at extreme conditions. Earth-Science Reviews 165, 185–202.
Van Westrenen, W., Frank, M.R., Hanchar, J.M., Fei, Y., Finch, R.J., Zha, C.S., 2004. In situ determination of the compressibility of synthetic pure zircon (ZrSiO4) and the onset of the zircon-reidite phase transition. American Mineralogist 89, 197–203.
Verma, S.K., Verma, S.P., Oliveira, E.P., Singh, V.K., Moreno, J.A., 2016. LA-SF-ICP-MS zircon U-Pb geochronology of granitic rocks from the central Bundelkhand greenstone complex, Bundelkhand craton, India. Journal of Asian Earth Sciences 118, 125–137.
Vishnevsky, S., Montanari, A., 1999. Popigai impact structure (Arctic Siberia, Russia): geology, petrology, geochemistry, and geochronology of glass-bearing impactites. In: Dressler, B.O., Sharpton, V.L. (Eds.), Large Meteorite Impacts and Planetary Evolution II. Special Paper 339. Geological Society of America, Boulder, pp. 19–60.
Wiedenbeck, M., Alle, P., Corfu, F., Griffin, W.L., Meier, M., Oberli, F., Quadt, A.V., Roddick, J.C., Spiegel, W., 1995. Three natural zircon standards for U-Th-Pb, Lu-Hf, trace element and REE analyses. Geostandards and Geoanalytical Research 19 (1), 1–23.
Wittmann, A., Kenkmann, T., Schmitt, R.T., Stöffler, D., 2006. Shock-metamorphosed zircon in terrestrial impact craters. Meteoritics and Planetary Science 41, 433–454.

Web references

http://www.unb.ca/passc/ImpactDatabase/.
georem.mpch-mainz.gwdg.de.
rruff.info.